The petrology, geochemistry, and age of lunar regolith breccias Miller Range 090036 and 090070: Insights into the crustal history of the Moon

A. CALZADA-DIAZ[1,2,*], K. H. JOY[3], I. A. CRAWFORD[1,2], and S. STREKOPYTOV[4]

[1]Department of Earth and Planetary Sciences, Birkbeck College, London WC1E 7HX, UK
[2]Centre for Planetary Sciences UCL/Birkbeck, London WC1E 7HX, UK
[3]School of Earth and Environmental Sciences, University of Manchester, Manchester M13 9PL, UK
[4]Imaging and Analysis Centre, Natural History Museum, London SW7 5BD, UK
[*]Corresponding author. E-mail: acalza01@mail.bbk.ac.uk

ABSTRACT

Meteorites ejected from the surface of the Moon as a result of impact events are an important source of lunar material in addition to Apollo and Luna samples. Here, we report bulk element composition, mineral chemistry, age, and petrography of Miller Range (MIL) 090036 and 090070 lunar meteorites. MIL 090036 and 090070 are both anorthositic regolith breccias consisting of mineral fragments and lithic clasts in a glassy matrix. They are not paired and represent sampling of two distinct regions of the lunar crust that have protoliths similar to ferroan anorthosites. ^{40}Ar-^{39}Ar chronology performed on two subsplits of MIL 090070,33 (a pale clast impact melt and a dark glassy melt component) shows that the sample underwent two main degassing events, one at ~3.88 Ga and another at

~3.65 Ga. The cosmic ray exposure data obtained from MIL 090070 are consistent with a short (~8–9 Ma) exposure close to the lunar surface. Bulk-rock FeO, TiO_2, and Th concentrations in both samples were compared with 2-degree Lunar Prospector Gamma Ray Spectrometer (LP-GRS) data sets to determine areas of the lunar surface where the regolith matches the abundances observed on the sample. We find that MIL 090036 bulk rock is compositionally most similar to regolith surrounding the Procellarum KREEP Terrane, whereas MIL 090070 best matches regolith in the feldspathic highlands terrane on the lunar farside. Our results suggest that some areas of the lunar farside crust are composed of ferroan anorthosite, and that the samples shed light on the evolution and impact bombardment history of the ancient lunar highlands.

INTRODUCTION

Lunar meteorites are an important source of material from the Moon; they provide information about the geology and geochemistry of terrains different from regions sampled during the Apollo and Luna sample return programs (Korotev et al. 2003; Korotev 2005; Day et al. 2006; Joy and Arai 2013; Gross et al. 2014). Lunar meteorites are ejected from the lunar surface by impacts that form shallow craters and expel material from the uppermost layer of the crust (Warren 1994; Basilevsky et al. 2010). Eventually, part of this material may fall on the Earth after some time traveling through the Earth's vicinity, typically this travel time is <5 million years (Myr) (Nishiizumi and Caffee 2013). It is thought that all meteorites recovered on Earth's surface arrived here within the last 2 Myr (Korotev 2005). According to the Meteoritical Bulletin Database (http://www.lpi.usra.edu/meteor/metbull.php), there are 262 lunar stones recovered up to September 22, 2016.

Chemically, there are three lithological types of lunar meteorites: brecciated anorthosites with bulk-rock compositions of 26–31 wt% Al_2O_3, 3–6 wt% FeO, and low concentrations of incompatible trace elements (<1 ppm Th); crystalline and brecciated basalts with bulk-rock compositions of 8–10 wt% Al_2O_3, 18–22 wt% FeO, and incompatible trace elements (0.4–2 ppm Th); and intermediate impact-melt, regolith, and fragmental breccias of noritic composition with bulk-rock compositions of 11–25 wt% Al_2O_3, 7–17 wt% FeO, and high concentration of incompatible elements (>3.5 ppm Th; Korotev 2005).

Regolith breccias are formed from unconsolidated fine-grained material that has been lithified by shock compression during impact events (McKay et al. 1986; Spray 2016). They are complex mixtures of different mineral and rock fragments derived from a range of different protolith environments. They represent regolith formation of different periods of lunar history, and form an archive of both lunar and wider solar system history (McKay et al. 1986; Joy et al. 2011a, 2011b, 2011c; Fagan et al. 2014; Wieler 2016). Lunar meteorite regolith breccias provide insights into the composition of different regions of the Moon and give an estimate of the typical composition of the upper crust (Palme et al. 1991; Warren 1994; Korotev et al. 2003; Warren et al. 2005; Joy et al. 2010; Korotev and Zeigler 2015). They are not only a valuable source of compositional information, but are also used as "ground-truth" for orbital remote sensing instrumentation (Korotev et al. 2003; Gillis et al. 2004; Korotev 2005; Warren et al. 2005; Korotev and Zeigler 2015).

Miller Range (MIL) 090036 and 090070 are two recently discovered lunar meteorites, classified as feldspathic regolith breccias. Both stones were found during the 2009–2010 Antarctic Search for Meteorites (ANSMET) field season in Antarctica (Righter 2010; Korotev and Zeigler 2015). In this paper, we report the bulk element composition, mineral chemistry analysis, and petrography of MIL 090036 and MIL 090070, as well as Ar-isotope age analysis for MIL 090070, to provide insights into their possible launch locations and geological evolution.

SAMPLES AND METHODS

The Meteoritic Working Group at NASA Johnson Space Center (MWG) provided two chips (MIL 090036,32 and MIL 090070,33; weighing 217 mg and 275 mg, respectively) and two polished thick (100 μm) sections (MIL 090036,34 and MIL 090070,35) mounted in epoxy resin blocks. A split of 150 mg of each chip was powdered using an agate mortar in a class 1000 clean room environment to avoid external contamination.

Mineral Chemistry

The thick sections were carbon coated and backscattered electron (BSE) images and mineral chemistries were obtained using a Cameca SX100 electron microprobe at the Natural History Museum (NHM), London and a Jeol8100 Superprobe with an Oxford Instrument INCA microanalytical system (EDS) at Birkbeck College. The instruments were operated at 20 keV accelerating voltage with a 20 nA beam current with a focused beam analysis for 10–30 s count time per element. Mineral chemistry data are reported in Appendix S1 in supporting information.

Qualitative element concentration and backscattered electron images were collected at a 256 × 256 pixels resolution using a Zeiss EVO EDS SEM at the NHM. Both instruments were calibrated using well-characterized standards. Element maps were subsequently processed using the GNU Image Manipulation Program (GIMP). The element maps were colorized and then combined using the program's function "Addition" tool to create false-color element maps (see approach of Snape et al. 2011).

Modal mineralogy of clasts was determined from BSE images using GIMP. Individual phases within each clast were automatically identified based on the grayscale tone in the BSE images. Modal abundances by area were calculated by counting pixels associated with each mineral phase within each clast. The major source of uncertainties in this method of calculating modal mineralogy occurs in distinguishing phases with similar grayscale tones in the BSE images (e.g., pyroxene and olivine), or in very compositionally zoned phases. In these cases, it was necessary to then also use the elemental maps to refine the selection.

Bulk-Rock Chemistry

Bulk-rock concentrations of major and minor elements (except Mn and K) were determined by inductively coupled plasma atomic emission spectrometry (ICP-AES) at the NHM using a Thermo Scientific iCap 6500 Duo ICP Spectrometer. The samples were dried at 105 °C and a 40 mg subsplit of each homogenized sample powder was pretreated with 0.5 mL concentrated HNO_3 (SpA™ grade, ROMIL Ltd) and fused with 120 mg of $LiBO_2$ (Spectroflux™ 100A, Alfa Aesar) in a Pt/Au crucible. The fused beads were dissolved in 40 mL 10% HNO_3 and made up to 100 mL with Milli-Q water. Calibration was performed using certified reference materials (CRM) prepared in the same way: AGV-2, BCR-2, DTS-1, GSP-2, and STM-1 (andesite, basalt, dunite, granodiorite, and syenite, USGS); JG-1 and JDo-1 (granodiorite and dolomite; GSJ, Japan), NIM-G, NIM-S, and NIM-P (granite, syenite, and pyroxenite; NIM, South Africa), MRG-1 (gabbro; CCRMP, Canada), AC-E (granite, GIT-IWG); and a candidate reference material DBC-1 (Ball Clay, IAG). Calibration curves were calculated using up to 13 points for each element. Each sample was analyzed in triplicate and the reproducibility for each major element was always better than 0.7%, and for P_2O_5—better than 3%. Accuracy was checked by the analysis of a CRM BHVO-2 (basalt, USGS) and a candidate reference material TML-1 (tonalite, IAG) and was within 1.1% of recommended values for all major elements and within 1.5% for P_2O_5.

Bulk-rock concentrations of trace elements, as well as Mn and K were determined by inductively coupled plasma–mass spectrometry (ICP-MS) at the NHM using an Agilent 7700x ICP mass spectrometer. An aliquot of 40 mg of each sample was pretreated with 1 mL of concentrated HNO_3 and dissolved in a mixture of 4 mL HF and 1 mL $HClO_4$ (all acids were SPA™ grade, ROMIL Ltd) in a closed 60 mL Savillex™ vial at 100 °C. This solution was dried down at 150 °C and the residue redissolved at 150 °C using 1 mL $HClO_4$. The solution was again dried down and then, redissolved in a mixture of 2 mL concentrated HNO_3 + 5 mL H_2O + 0.1 mL H_2O_2 (Suprapur Merck) at 70 °C and afterward made up to 40 mL with water. Analytical blanks were prepared in triplicate. Samples were analyzed in triplicate for most elements; the reproducibility being better than 1% for about half of the trace elements and better than 5% for all other elements apart from Cd, Cs, and Tl. The analytical accuracy was checked using CRMs JLs-1 and JLk-1 (limestone and lake sediment, GSJ), and BCR-2 and DNC-1 (basalt and dolerite, USGS; see data table in Appendix S1). For most elements, the concentrations found in the CRMs were within the uncertainty of the recommended values.

Argon Chronology

^{40}Ar-^{39}Ar age determinations were performed using stepped laser heating of two subsplits of bulk sample MIL 090070,33. These are named MIL 090070,33 "dark melt" (1.28 mg mass) removed from an area of dark glassy matrix melt, and MIL 09007,33 "pale melt" (3.18 mg mass) removed from a pale impact-melt breccia clast.

Samples were irradiated at the Oregon State University Radiation Center. Aliquots of Hb3gr monitor (1080.4 1.1 Ma; Renne et al. 2010) were positioned in close proximity (few mm) to the samples which were irradiated in silica glass vials. The **J** value, a parameter that is representative of the neutron irradiation conditions, was 0.08018 0.00113 (1**r**) (1.41%). Stepped heating was performed using a Photon Machines Fusions IR 10.6 **l**m wavelength CO_2 laser coupled to a Thermo Scientific™ Argus VI preparation bench and ulticollector mass spectrometer at the University of Manchester. The sample was lasered using a 3 mm defocused beam for 30 s with increasing output power at each step (see Table 1 for details) until the sample was degassed. The released gas was cleaned for 2 min on a hot getter, and then 1 min on a hot and cold getter prior to introduction to the mass spectrometer. Isotopes were measured simultaneously and in peak jumping mode: ^{40}Ar, ^{38}Ar, and ^{37}Ar were measured on Faraday cups and ^{39}Ar and ^{36}Ar on a Compact Discrete Dynode (CCD) detector. Data have been corrected for blank contribution, mass discrimination, neutron-induced interference isotope production on ^{40}Ar, ^{39}Ar, ^{38}Ar, and ^{36}Ar and decay of ^{37}Ar and ^{39}Ar, and using the decay constants of Renne et al. (2010). ^{40}Ar-^{39}Ar age steps provided in Table 1 with two standard deviation (2**r**) level of analytical uncertainty, and fusion ages and plateau calculations are presented with internal and external errors. The Isoplot v4 (after Ludwig 2012) Excel plugin was used to produce data plots. Exposure ages were calculated using the ratio of cosmogenic ^{38}Ar (from the relationship $^{38}Ar_c$ = (5.35**9**^{38}Ar-^{36}Ar)/(5.35–0.65): where 5.35 is the trapped $^{36}Ar/^{38}Ar$ solar wind ratio and 0.65 trapped $^{36}Ar/^{38}Ar$ cosmogenic ratio of Hennessy and Turner 1980) to the concentration of ^{37}Ar derived from Ca (Table 1). $^{38}Ar_c/^{37}Ar$ ratios then provide apparent cosmic ray exposure (CRE) ages using the bulk sample chemistry, and P38 2p cosmogenic production rates of Eugster (1988). Error on exposure age steps reported include the internal uncertainty on J, and an approximate 10% error on the P38 value.

RESULTS

Petrography

MIL 090036,34 (Figs. 1a and 1b) is a feldspathic polymict regolith breccia with a fine-grained to glassy matrix. The section studied has clasts that range from <0.1 mm to 2 mm in size. These clasts are mostly monomictic plagioclase grains and impact-melt breccias (Fig. 2a), but a significant number of clasts of granulitic breccias with olivine (Fig. 2b; grain size up to 60 μm), some annealed granulitic breccias with ilmenite (Fig. 2c), and rarer fine-grained granulitic breccias (Fig. 2d; grain size <5 μm) are also present. The clast-bearing impact-melt breccia clasts (Figs. 2e–g) have the largest sizes (up to 3 mm). Sparse clasts of poikiloblastic impact-melt breccias were also found (Fig. 2h). All the clasts are embedded in a fine-grained to glassy matrix, which is dark colored in hand specimen.

Table 1. *Bulk-rock major element (wt%) and trace element (ppm) compositions of MIL 090036,32 and MIL 090036,32 and MIL 090070,33 obtained in this study ± their analytical errors (1 SD). Previous analyses of these samples, their paired stones, and Apollo 16 have been included for comparison. Missing values in the table indicate that the values are not reported in the literature. Average FeO, TiO_2 and Th ± 2 standard deviation uncertainties used for suggesting the possible launch origin of MIL 090034, 090070, 090075 are also shown.*

	MIL 090036 (this work)	MIL 090036 (Korotev and Zeigler 2015)	Apollo 16 Soils (Jolliff et al. 2006)	MIL 090070 (this work)	MIL 090070 (Korotev and Zeigler 2015)	MIL 090034 (Korotev and Zeigler 2015)	MIL 090075 (Korotev and Zeigler 2015)
Al_2O_3	26.72	27.10	26.70	30.72	31.30	31.00	29.80
CaO	15.45	15.50	15.30	17.45	17.00	17.10	16.60
FeO	5.27	5.01	5.44	3.77	3.26	3.40	3.70
K_2O	0.08	0.10	0.12	0.03	0.04	0.03	0.06
MgO	5.92	5.18	6.00	2.98	2.75	2.84	3.85
MnO	0.07	0.07	0.07	0.05	0.05	0.05	0.05
Na_2O	0.57	0.62	0.46	0.37	0.37	0.37	0.39
P_2O_5	0.08	0.10	0.12	0.02	0.02	0.02	0.06
SiO_2	46.24	45.40	44.90	45.16	44.50	44.30	45.20
TiO_2	0.48	0.57	0.59	0.16	0.14	0.15	0.21
Cr_2O_3		0.10	0.11		0.06	0.07	0.08
Total	100.88	99.75	99.81	100.69	99.49	99.33	100.00
Mg#	66.68	64.80	66.00	61.07	60.10	59.80	65.00
La	10.63	11.11	13.00	2.99	2.15	1.80	6.78
Ce	26.67	29.00	34.00	6.24	5.38	4.72	17.20
Pr	3.62		4.50	0.98			
Nd	16.46	17.20	21.00	4.41	3.31	2.99	10.40
Sm	4.65	5.04	6.00	1.28	0.98	0.86	3.02
Eu	1.47	1.38	1.20	0.99	0.86	0.84	0.94
Gd	5.57		8.00	1.55			
Tb	0.96	0.98	1.20	0.26	0.20	0.18	0.61
Dy	6.20		8.00	1.77			
Ho	1.29		1.70	0.37			
Er	3.69		5.00	1.06			
Tm	0.53		0.70	0.16			
Yb	3.30	3.25	4.30	0.99	0.78	0.70	2.22
Lu	0.48	0.45	0.61	0.14	0.11	0.10	0.30
Li	7.08		8.00	2.99			
Be	0.89			0.28			
K	687.11		1010.00	212.94			

Sc	11.82	9.77	9.50	6.81	6.29	6.62	6.90
V	25.68		25.00	14.76			
Cr	760.51		760.00	463.47			
Mn	566.46		540.00	381.99			
Co	22.62	17.80	21.00	9.39	8.10	8.10	11.10
Ni	381.45	218.00	440.00	52.04	43.00	45.00	83.00
Cu	3.80			2.77			
Zn	14.82		26.00	5.85			
Ga	4.32		3.60	3.27			
Rb	2.06		2.90	0.56			
Sr	197.34	198.00	176.00	168.07	161.00	159.00	162.00
Y	29.70		46.00	9.02			
Zr	128.84	153.00	180.00	33.43	27.00	24.00	94.00
Nb	8.55		13.00	2.10			
Mo	0.13			0.04			
Ag	<0.013			<0.013			
Cd	0.04			0.02			
Sn	<0.3			<0.3			
Sb	1.20			0.11			
Cs	0.09		0.14	0.02			
Ba	116.87	131.00	140.00	32.45	27.00	26.00	78.00
Hf	3.74	3.86	4.50	0.95	0.66	0.62	2.31
Ta	0.49	0.44	0.55	0.12	0.08	0.08	0.26
W	0.24	<0,5		0.06			
Tl	0.01			0.01			
Pb	1.40			0.35			
Th	1.89	1.65	2.2	0.44	0.32	0.28	1.11
U	0.52	0.46	0.62	0.13	0.13	0.07	0.33

***Table 1**. Continued. Bulk-rock major element (wt%) and trace element (ppm) compositions of MIL 090036,32 and MIL 090070,33 obtained in this study their analytical errors (1 SD). Previous analyses of these samples, their paired stones, and Apollo 16 have been included for comparison. Missing values in the table indicate that the values are not reported in the literature. Average FeO, TiO_2, and Th 2 standard deviation uncertainties used for suggesting the possible launch origin of MIL 090034, 090070, 090075 are also shown.*

Three types of granulitic breccias have been found in this section: gabbroic granulitic breccias with olivine (Fig. 2b), recrystallized granulitic breccias with ilmenite (Fig. 2c), and fine-grained granulites (Fig. 2d).

The gabbroic granulitic breccias (Fig. 2b) are mainly formed of plagioclase, clinopyroxene, and olivine. They vary significantly in size, reaching up to 1 mm, and have irregular shapes. The plagioclase (~85% modal area) is calcic, varying between An_{83} and An_{96} (Fig. 3, yellow square symbols). Commonly, the crystals are highly fractured and also show some regions of remelting, and possible maskelynitization, mainly in the borders of the clasts. Crystals of pyroxene (~10% modal area) are both augite ($En_{46–49}$ $Fs_{13–15}$ $Wo_{36–41}$) and pigeonite ($En_{63–64}$ $Fs_{26–29}$ $Wo_{5–11}$; Fig. 4, diamond symbols), between 12 **l**m and 90 **l**m in size with anhedral to subhedral crystals. The olivine crystals (~5% modal area) show less size variation (~8 **l**m). They have subhedral textures and are relatively equilibrated with $Fo_{66–67}$.

Annealed granulitic breccias with ilmenite are composed of calcic plagioclase (~90% modal area) with clinopyroxene (<10% modal area) and variable amounts of ilmenite (<1% modal area and 4–58 **l**m in size; Fig. 2c). The clasts are heavily recrystallized, have an irregular shape, and range from ~0.8 mm to ~2 mm in size. Plagioclase crystals (~77% modal area) reach up to 400 **l**m in length and their compositions vary from An_{84} to An_{94}. They are highly fractured and occasionally have been transformed into glass, probably maskelynite. Pyroxenes (~22% modal area) are poorly sorted (sizes from sub-micron to 165 **l**m), anhedral to

lath-like in form, and consist of pigeonite ($En_{59–61}Fs_{27–31}$ $Wo_{6–13}$), augite ($En_{35–49}$ $Fs_{15–25}$ $Wo_{33–40}$) and lesser amounts of enstatite ($En_{56–69}$ $Fs_{27–39}$ $Wo_{4–5;}$ Fig. 4, blue square symbols). Rare ilmenite crystals (~1% modal area) are observed within these clasts, they are blocky with sizes from submicron to ~60 1m.

Fine-grained granulite clasts (Fig. 2d) are scarce within this subsample. They consist of >90% modal area of calcic plagioclase, which encases small (<5 1m) grains of pyroxene.

Clast-bearing impact-melt breccias are abundant within MIL 090036,34. They all show similar textures although they have different makeup of mineral and clast components. They are clast-rich with a recrystallized matrix composed of quenched plagioclase laths in a mafic glass (Fig. 2e, f) or a feldspathic glass matrix (Fig. 2g). The clasts in these impact melts are mainly fragments of poorly sorted plagioclase (>50% modal area of the clasts; up to 600 1m) with a narrow range of compositions ($An_{92–95}$; Fig. 3, red triangle symbols) and show a range of shock states. Plagioclase fragments in the recrystallized matrix have a composition between An_{90} and An_{98}. One of the impact-melt breccias, however, contains an alkali-rich plagioclase clast ($An_{59–63}$; Fig. 3, green diamond symbols) ~500 1m across (labeled pl in Fig. 2f); this suggests a different type of parent lithology.

Poikiloblastic impact-melt clasts have been found in MIL 090036,34 (Fig. 2h). They are formed of plagioclase (~90% modal area), clinopyroxene (~10% modal area), and rare grains of Fe-Ni metal (<1% modal area). This metal indicates that the clasts were probably derived from an impact-melt precursor, as it was likely added by a meteoritic component. The clinopyroxene (pigeonite and augite) are large (from ~100 µm to ~400 µm) anhedral crystals with poikiloblastic texture. Anhedral to subhedral plagioclase grains of medium size (~20 µm to ~75 µm) are included in the clinopyroxene crystals. Enclosing these phases are larger crystals of plagioclase (up to ~220 µm, An_{83} to An_{96}: Fig. 3, blue triangle symbols) with some regions transformed into maskelynite with a similar composition.

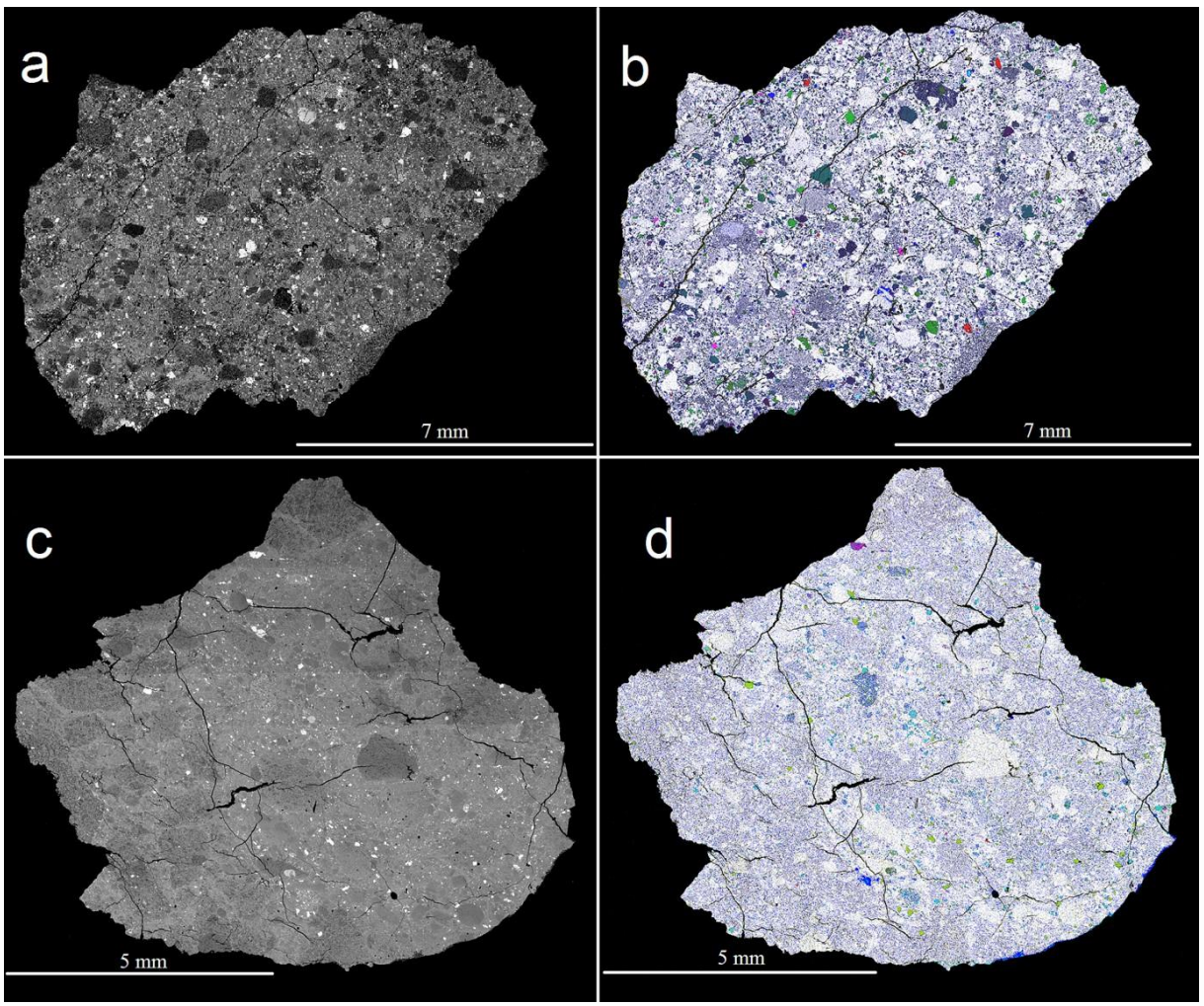

***Fig. 1**. BSE image of MIL 090036, 34 (a). False-color element map of MIL 090036, 34 showing distribution and qualitative concentration of elements present (b). BSE image of MIL 090070, 35 (c) and false-color element map of MIL 090070, 35 (d). The maps have been colored Si-blue, Al-white, Ca-yellow, Mg-green, Fe-red, Ti-pink, and K-cyan following method of (Joy et al. 2011a, 2011b, 2011c; Snape et al. 2011).*

The matrix of the MIL 090036,34 sample comprises glass and fine-grained plagioclase, pyroxene, and ilmenite and includes minor amounts of small (<30 μm) quartz, chromite, and Fe-Ni metal grains. MIL 090070,35 (Figs. 1c and 1d) is dominated by clast-rich impact-melt breccias (Figs. 5a and 5b), anorthositic clasts (Fig. 5c), annealed clasts (Fig. 5d), and mineral fragments of pyroxene and olivine on a glassy matrix.

Impact-melt breccia clasts (Figs. 5a and 5b) are variable in size, some of them up to 3 mm, showing angular shapes and poorly defined borders that merge into the meteorite matrix. Most impact-melt breccias are feldspathic in composition, containing poorly sorted plagioclase fragments up to 500 μm forming >90% modal area. Other impact-melt breccia clasts in the meteorite contain a more mafic assemblage of pigeonite and augite (~20% modal area) and plagioclase (>80% modal area; Fig. 5b).

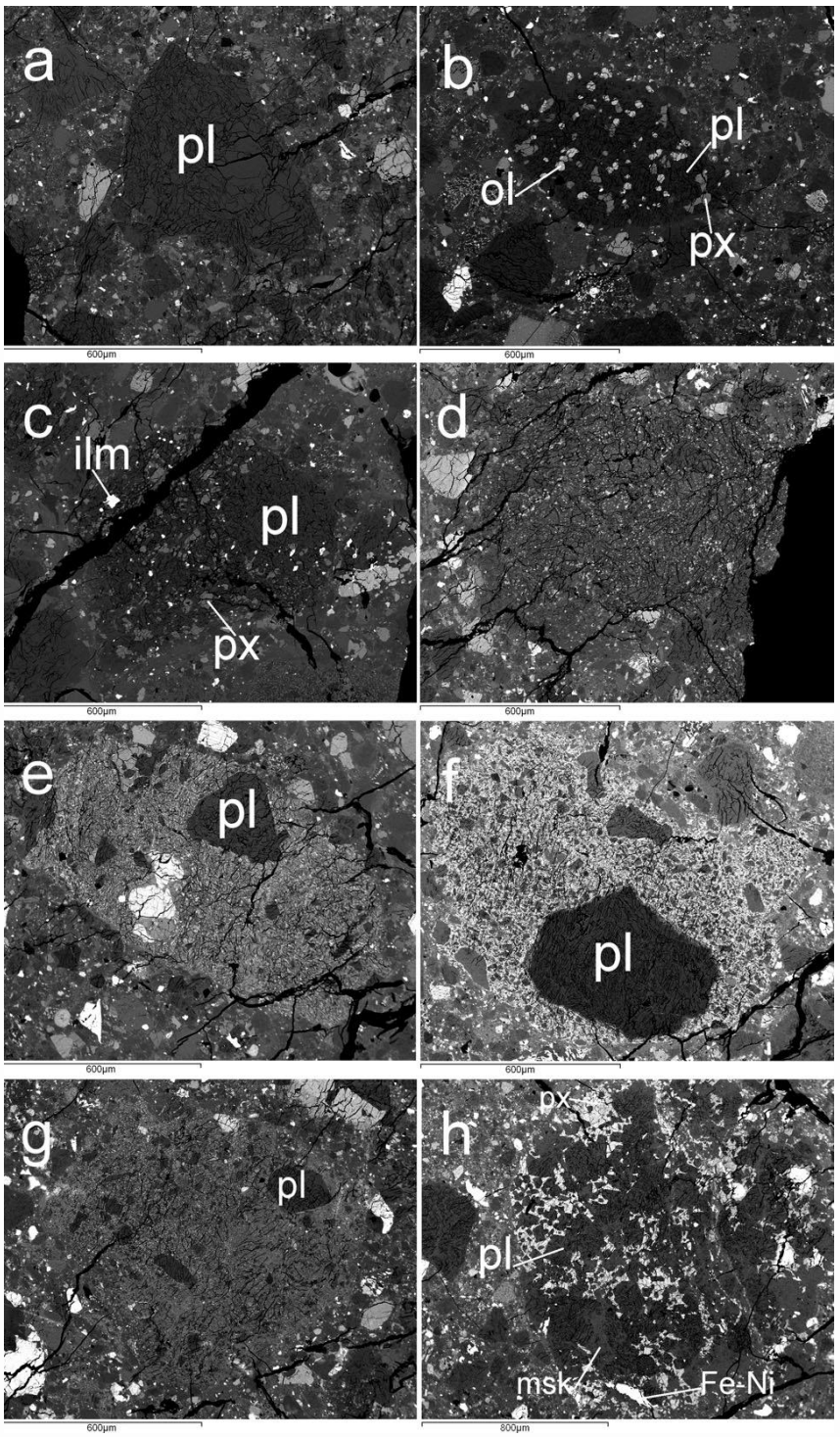

Fig. 2*. BSE images of different clasts observed in MIL 090036,34. Anorthositic clast (a); gabbroic granulitic breccia (b); recrystallised granulitic breccia (c); fine-grained granulite (d); impact-melt breccia clast (e); impact-melt breccia clast (f, g); poikiloblastic impact-melt clast (h). The large anorthositic clast in (f) has a composition An56 (see Fig. 3), other smaller mineral fragments within the matrix of this clast also show high alkali signature.*

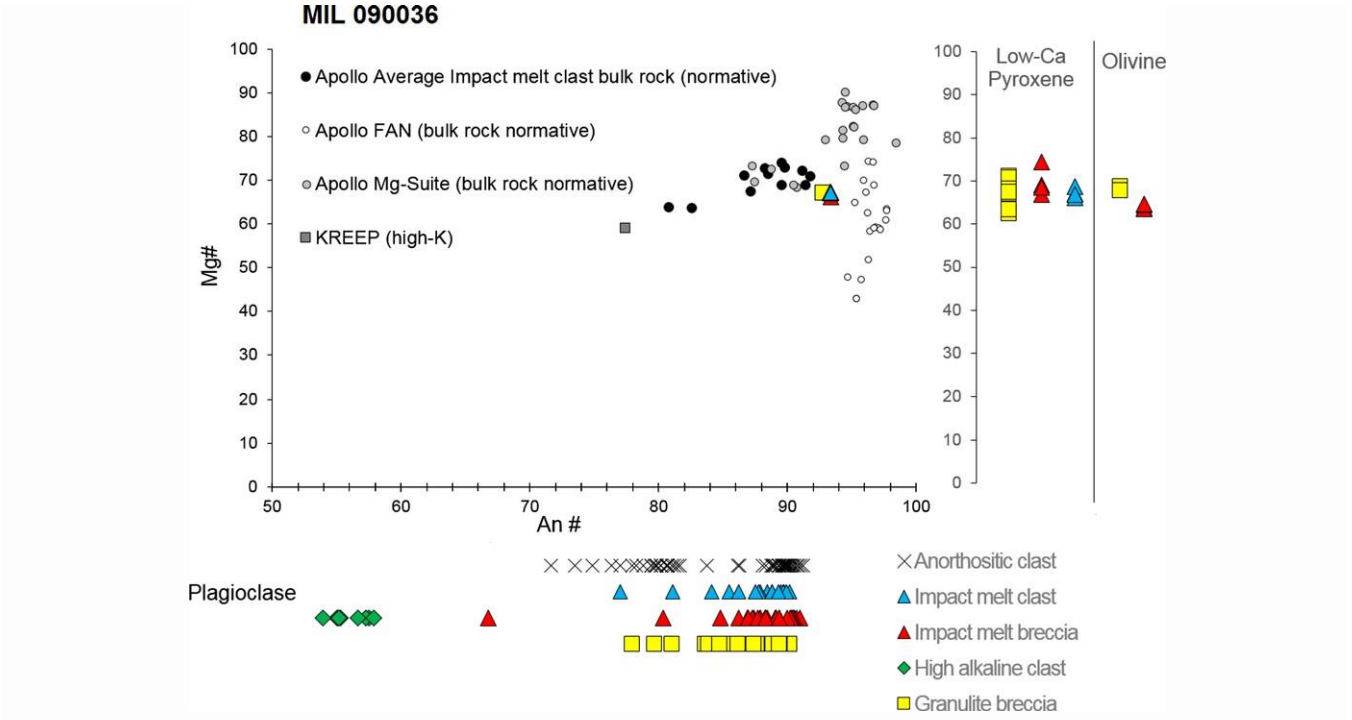

Fig. 3. *MIL 099036 An# (molar Ca/(Ca + K + Na) ⨀ 100) versus Mg# (molar Mg/(Mg + Fe) ⨀ 100) plot for averaged plagioclases, low-Ca pyroxenes, and olivines from granulite breccias, impact-melt breccias, and impact melts compared to the Apollo rock suites (Korotev 1996; Jolliff 1998). The range of individual clast and matrix Mg# mafic mineral compositions is shown at right, and An# plagioclase composition is shown under the main figure.*

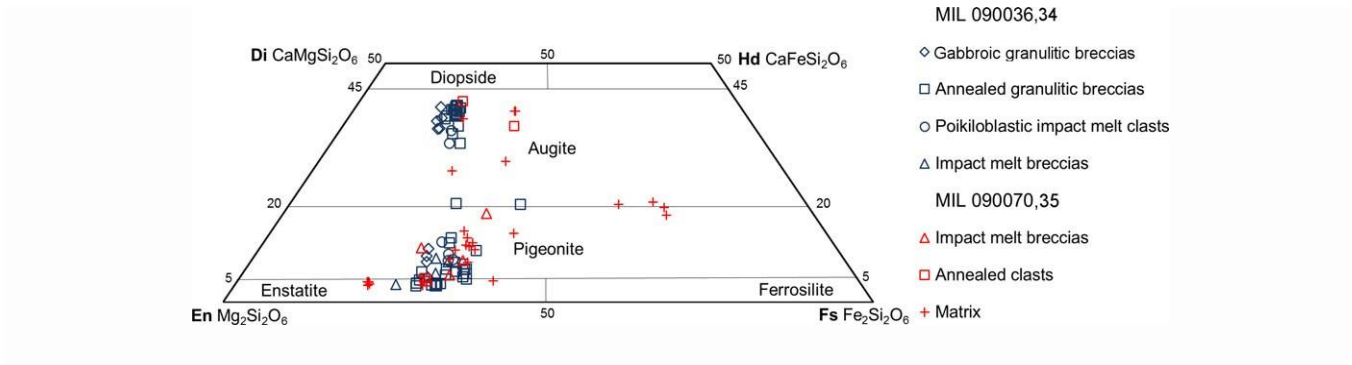

Fig. 4*. Pyroxene quadrilateral diagram showing compositions of pyroxenes in clasts from samples MIL 090036,34 and MIL090070,35.*

Plagioclase fragments (Fig. 5c) occur within the matrix in various sizes up to 1 mm. These clasts ($An_{93–98}$; Fig. 6, cross symbols) are similar in composition to those clasts found in the impact-melt breccias ($An_{91–98}$; Fig. 6, red triangle symbols), suggesting a similarity of parent lithology. Plagioclase grains in the monomictic fragments in MIL 090070 often appear highly fractured and transformed into maskelynite (see also Martin et al. 2016).

Annealed impact-melt clasts (Fig. 5d) are scarce within the sample and contain plagioclase (~75% modal area and An_{90} to An_{95}; Fig. 6, blue diamond symbols) and pyroxene (~25% modal area and $En_{56–65}$ $Wo_{4–11}$ $Fs_{31–35}$; Fig. 4, red square symbols).

The matrix of MIL 090070,35 hosts pyroxene and olivine crystals (<0.2 mm in size). Pyroxene crystals are anhedral and are highly variable in composition, ranging from enstatite to pigeonite to augite ($En_{22–75}$ $Wo_{3–42}$ $Fs_{16–59}$). Olivine crystals are scarce; they are anhedral to subhedral and their compositions range between Fo_{49} and Fo_{70}. No mare basaltic or KREEP-rich (acronym for K, REE, and P) clasts were found within MIL 090070,35.

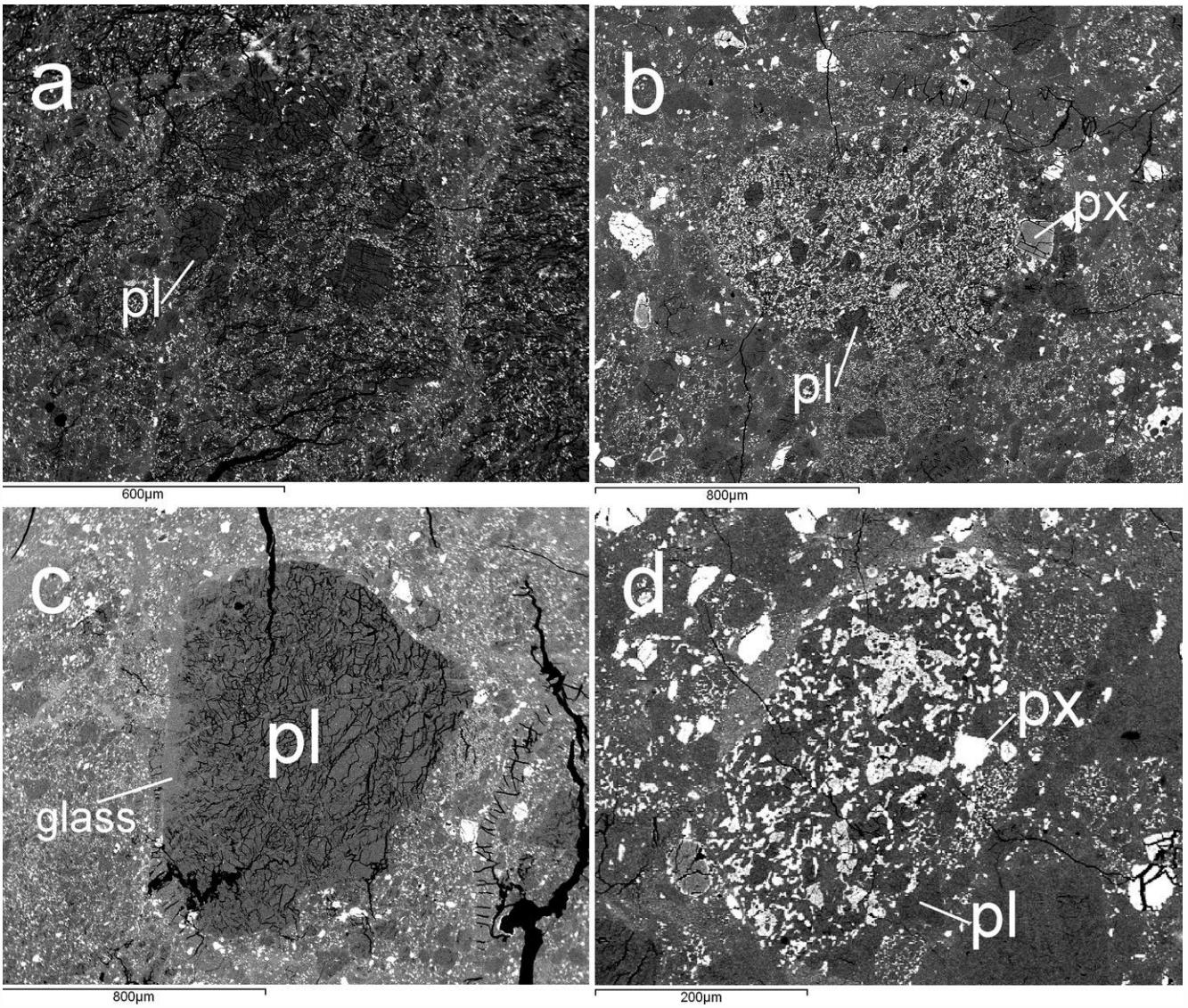

Fig. 5*. BSE images of different clasts observed in MIL 0900701,35. Impact-melt breccia (a, b); anorthositic clast (c); annealed clast (d).*

Bulk Chemistry

Our results (Table 1) are very similar to those reported previously by Korotev and Zeigler (2015). MIL 090036 has an enhanced KREEP component (Fig. 7) as indicated by higher concentrations of incompatible elements (Th 1.9 ppm; Sm 4.65 ppm), compared to MIL 090070 (Th 0.4 ppm; Sm 1.28 ppm). Bulk-rock composition of MIL 090070 (Table 1) is more feldspathic and ferroan: 30.7 wt% Al_2O_3, 3.4 wt% FeO, and Mg# (MgO/(MgO + FeO) molar) 61 compared with MIL 090036 (26.7 wt% Al_2O_3, 5.3 wt% FeO and Mg# 67).

Argon Chronology

Two subsamples from MIL 090070,33 were analyzed for argon isotopes. A subsample weighing 3.18 mg was composed of one of the feldspathic impact- melt breccia clasts and is referred to as "pale melt." A subsample weighing 1.28 mg was composed of dark, glassy melt matrix and is referred to as "dark melt." Both of these melt subsamples contain a range of small minerals (plagioclase, pyroxene, and olivine) and glass. Results are listed in Table 2.

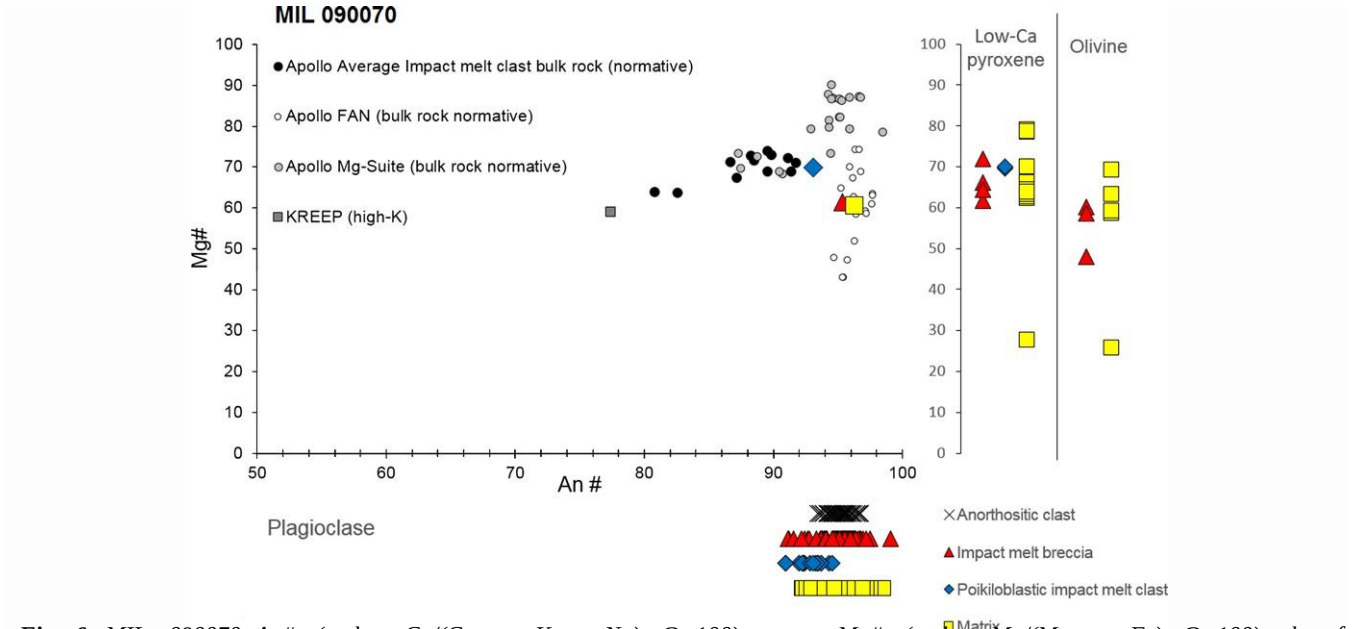

Fig. 6. *MIL 090070 An# (molar Ca/(Ca + K + Na) 9 100) versus Mg# (molar Mg/(Mg + Fe) 9 100) plot for averaged plagioclases, low-Ca pyroxenes, and olivines from granulite breccias, impact-melt breccias, and impact melts compared to the Apollo rock suites (Korotev 1996; Jolliff 1998). The range of individual clast and matrix Mg# mafic mineral compositions is shown at right, and An# plagioclase compositions is shown under the main figure. Note that the high alkaline clast is a component of an impact-melt breccia.*

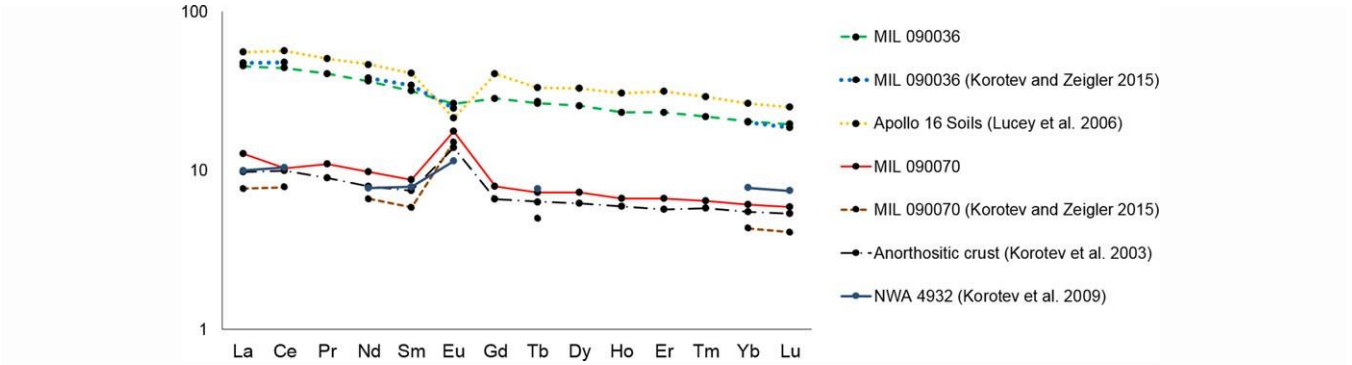

Fig. 7. *CI-normalized (Anders and Grevesse 1989) rare earth elements abundances for MIL 090036 and MIL 090070 (Table 1), Apollo 16 soils, lunar meteorite NWA 4932, and the calculated upper lunar feldspathic crust (Korotev et al. 2003, 2009; Lucey et al. 2006; Korotev and Zeigler 2015).*

Pale Clast

From the summed ^{40}Ar and ^{37}Ar measurements (Table 2) we can calculate equivalent CaO and K_2O compositions. The bulk CaO of the pale clast (13.44 0.11 wt% 2**r**) is lower than the MIL 090070 bulk-rock composition (17.45 0.045 wt% CaO), and the K_2O of the clast (0.0256 0.002 wt% 2**r**) is similar to the bulk rock (0.0257 0.0004 wt% K_2O). With increasing temperature steps different minerals and phases (i.e., plagioclase, pyroxene, olivinem glass) release gas and we see that the K/Ca ratio varies between 0.001 and 0.002 (see Fig. 9). The highest temperature gas releases K/Ca ratios of 0.001 are consistent with pyroxene mineral gas releases (Fig. 4). The first two and last temperature release steps showed high $^{38}Ar/^{36}Ar$ ratios (>3) (Table 2), suggesting an added Cl-rich component from terrestrial contamination.

Most of the other extractions give $^{38}Ar/^{36}Ar$ ratios of 1–2 (Table 2), consistent with being dominated by a cosmogenic ^{36}Ar component rather than solar. No excess ^{40}Ar lunar atmosphere is present, consistent with the parent rock being buried at depths below the surface regolith levels.

The $^{39}Ar/^{40}Ar$ versus $^{36}Ar/^{40}Ar$ ratios for the pale clast are displayed in Fig. 8 where an isochron has been fitted to the high-temperature step data to investigate initial trapped $^{40}Ar/^{36}Ar$ components. These isochrons also indicate that there is essentially no trapped solar wind component in the sample, as the $^{40}Ar/^{36}Ar$ intercept isochron gives a negative value with a large uncertainty. Isochron model age fits are shown in Fig. 9; however, they are not significant,

given clustering at the radiogenic endmember. Higher $^{40}Ar/^{36}Ar$ values (>400) for individual steps were reported by Park et al. (2013) from analysis of MIL 090070 bulk rock.

Assuming that a solar wind or trapped component correction is present, then a release step model profile is shown in Fig. 9. The Ar-Ar age increases uniformly with extraction temperature and shows a partial Ar degassing profile. The sample has experienced low- temperature diffusion (equivalent to 0–43% ^{39}Ar loss)^{40}Ar loss, typical of lunar samples. This can be caused either by heating or by a low-level impact. No well-defined plateau age was observed (see Fig. 9). Summing together the last high-temperature release steps equivalent of 58% of ^{39}Ar release to gives a summed gas release model age of 3653 65 Ma (2σ) (Table 2). This may correspond to the lower limit to the Ar degassing age, as some ^{40}Ar could have been lost by diffusion from these high temperature lattice sites. The cosmic ray exposure age of the sample is 8.4 1 Ma (2σ) (Table 2).

Dark Melt

From the summed ^{40}Ar and ^{37}Ar measurements (Appendix S1) we calculate that the dark melt clast has 14.05 0.40 wt% CaO and 0.026 0.001 K_2O wt% (2σ). These are similar to the pale clast component (Table 2), and again the clast CaO composition is slightly lower than the bulk-rock composition (Table 1).

The first two temperature steps have high $^{38}Ar/^{36}Ar$ ratios (>2), suggesting an excess Cl-derived ^{38}Ar component from terrestrial contamination in Antarctica. The fourth and fifth (10–12% of total ^{39}Ar release) low temperature ^{39}Ar release have $^{38}Ar/^{36}Ar$ ratios of 0.3, implying the presence of trapped Ar consisting of solar ^{36}Ar and ^{38}Ar and lunar atmosphere ^{40}Ar. The remainder of the ^{39}Ar released has $^{38}Ar/^{36}Ar$ ratios of 0.8–1 suggesting a mix of solar and cosmogenically contributed ^{36}Ar and ^{38}Ar. This indicates that the glassy melt material experienced limited exposure at the lunar surface.

To correct for cosmogenically contributed ^{36}Ar, the $^{38}Ar/^{36}Ar$ ratio was used to divide the ^{36}Ar into cosmogenic and trapped components, and we removed the cosmogenic component. This correction is appropriate for all steps apart from the first two, which are affected by terrestrial excess Cl-derived ^{38}Ar. Only calculated ^{36}Ar concentrations from trapped solar wind were used to construct the isochron plots (see approach of Nyquist et al. 2006) and the reported age data (Table 2).

The $^{39}Ar/^{40}Ar$ versus ^{36}Ar (trapped)/^{40}Ar ratios from this portion are displayed in Fig. 8 where an isochron has been fitted to the high-temperature steps to investigate the initial $^{40}Ar/^{36}Ar$ values. However, all of the $^{36}Ar/^{40}Ar$ data sit close to the radiogenic component and these isochrons indicate that there is no significant trapped component in the sample as the $^{40}Ar/^{36}Ar$ (trapped) intercept is a negative value with large uncertainty. Therefore, the isochron model ages are not significant. $^{40}Ar/^{36}Ar$ (trapped) ratios for individual steps are high similar to those observed in the impact- melt breccia clast and other MIL feldspathic lunar meteorites reported by Park et al. (2013).

Trapped Ar in the lunar regolith typically has $^{40}Ar/^{36}Ar$ ratios of ~0.2–16 (Joy et al. 2011a, 2011b, 2011c, and references therein). However, correcting the data for this range of values does not change the step releases within the errors reported. Thus, we assume a $^{40}Ar/^{36}Ar$ ratio of 1 and the model plateau release profile is shown in Fig. 10. An apparent plateau age (where a plateau is defined as >60% of the ^{39}Ar release in three more contiguous steps) of 3877 160 Ma (2σ) is given by the final 81.9% release of ^{39}Ar (fusion ages are reported in Table 2). The cosmic ray exposure age is 9.0 ± 1.9 Ma (2σ) (Table 2).

EVIDENCE FOR LUNAR ORIGIN

The MIL 090036 bulk rock does not have an obvious fusion crust. However, it does show a thin ochre film on two surfaces that may be a weathered fusion crust (Righter 2010). The macroscopic description of MIL 090070 reports an olive-green glassy fusion crust (Righter 2010). The presumed fusion crust on MIL 090036 (later weathered by Earth's atmosphere) and the green crust on MIL 090070 appear to have been formed by frictional heating during passage through Earth's upper atmosphere, suggesting an extraterrestrial origin for both samples.

Both rocks also show a mineralogy different from that found in terrestrial rocks (i.e., presence of Fe-Ni metal, Ti-rich ilmenite, and lack of hydrous phases), indicating that the samples were formed in a highly reducing environment (Papike 1998). Fe/Mn ratios of pyroxenes and olivines vary between planetary bodies because of the original composition of accreted material, differentiation, and oxygen fugacity conditions, making them a useful tool to determine planetary origin (Papike 1998). Average Fe/Mn (atomic) values measured on pyroxene are 54.81 ± 0.51 (1 standard deviation, SD) for MIL 090036 and 62.67 ± 0.52 (1 SD) for MIL 090070; those for and o livine (97.48 ± 0.38 (1 SD) on MIL 090036 and 85.93 ± 0.62 (1 SD) on MIL 090070, all supporting a lunar origin (Papike 1998; Papike et al. 2003).

Table 2. *Miller Range 090070, 33 components ^{40}Ar-^{39}Ar analytical data calculated from each heating release step. Errors on individual steps and on the age calculation are given at the 2σ level of uncertainty; nd = not determinable*

Laser Power (W)	Concentration (moles) ^{36}Ar ($\times 10^{-18}$)	$^{36}Ar_{(trapped)}$ ($\times 10^{-18}$)	^{37}Ar ($\times 10^{-18}$)	^{38}Ar ($\times 10^{-18}$)	^{39}Ar ($\times 10^{-18}$)	^{40}Ar ($\times 10^{-18}$)
Pale Clast	mass = 0.00318 g					
0.26 W	7.44 0.36		102063 462	60.3 3.8	403.4 11.6	7505 14
0.83 W	31.42 4.74		446723 834	97.2 1.7	1562.3 16.2	47439 84
1.35 W	59.96 0.95		565107 1222	125.5 3.5	1820.6 26.0	104712 189
1.81 W	73.78 0.69		544823 1136	127.2 5.0	1646.0 23.7	125491 241
2.33 W	53.98 0.62		323199 855	86.2 4.2	909.2 19.6	72412 111
2.75 W	94.43 0.90		352038 787	98.8 4.9	1010.1 17.0	80741 160
3.52 W	100.12 0.66		375265 928	107.4 3.4	1077.3 20.9	87259 163
4.35 W	98.28 0.54		351920 763	106.4 3.3	1128.8 16.3	94423 172
4.82 W	64.60 0.53		238122 454	72.8 3.9	795.4 9.0	67011 114
5.23 W	46.98 0.41		185413 705	57.8 2.7	627.9 17.4	52935 107
5.8 W	44.86 0.68		215796 557	62.1 4.7	691.1 12.8	57877 104
6.27 W	31.99 0.50		180570 491	52.6 4.8	555.8 11.4	45698 82
6.94 W	6.32 0.64		31448 505	8.9 2.2	86.6 13.2	6871 27
7.56 W	19.26 0.49		133496 415	40.1 3.8	307.1 10.0	24299 35
8.19 W	13.99 0.34		94548 438	26.7 2.9	173.1 11.1	13396 21
8.7 W	2.20 0.23		13870 477	11.4 2.3	29.0 12.4	2237 11
Total	749.63 5.28		4154400 2930	1141.5 14.8	12823.8 65.1	890304 490
Dark Clast	mass = 0.00128 g					
0.21 W	2.36 0.31	-3.02 - 4.06	2788 528	7.7 4.7	14.5 13.8	560 9
0.62 W	8.61 0.34	-4.57 - 2.60	11348 624	19.4 3.0	56.9 16.3	2798 10
1.19 W	8.00 0.34	2.32 3.50	21068 523	9.2 4.0	85.8 13.6	3338 10
1.76 W	15.51 0.31	2.55 3.27	39212 503	20.4 3.8	144.2 13.1	9134 15
2.33 W	87.11 0.31	73.87 4.11	38195 474	34.2 4.7	138.8 12.3	32500 54
2.69 W	23.16 6.23	21.14 9.77	31749 301	7.1 2.2	105.4 7.8	10377 22
3.11 W	16.65 0.29	7.43 4.26	25378 203	15.6 4.9	81.1 5.3	9035 19
3.52 W	24.69 0.39	10.88 2.91	52342 345	23.3 3.3	158.7 8.9	15106 25
4.4 W	30.27 0.44	14.63 4.00	59584 287	26.8 4.6	174.6 7.3	15514 21
4.9 W	17.73 0.36	9.81 4.27	33503 355	14.0 4.9	97.7 9.2	8902 15
5.4 W	12.91 0.32	5.01 4.34	26424 267	13.1 5.0	74.7 6.9	6956 17
5.9 W	15.44 0.28	8.51 4.00	27964 445	12.3 4.6	81.4 11.6	8177 12
6.4 W	24.99 0.38	16.79 2.43	46859 458	15.8 2.7	141.0 11.9	12743 26
6.9 W	39.49 0.49	26.23 2.91	77325 393	25.3 3.3	230.9 10.0	20996 38
7.4 W	51.25 0.55	31.67 2.57	89311 403	36.0 2.8	272.8 10.2	26228 48
7.9 W	162.16 1.01	104.54 2.92	323272 845	108.2 2.9	974.7 19.6	91938 163
8.2 W	87.51 0.43	57.68 2.54	175794 523	56.7 2.9	533.5 12.5	50653 90
8.5 W	151.92 0.84	94.85 2.90	345992 1067	105.5 3.0	1029.0 25.7	98074 187
6.94 W	77.33 0.50	49.65 2.13	169229 502	51.9 2.3	490.0 11.9	47115 76
10 W	53.52 0.44	34.32 2.07	99981 610	36.0 2.3	295.4 15.6	28502 49
8.19 W	14.43 0.40	5.50 2.81	30348 409	14.8 3.2	87.4 10.6	8328 18
8.7 W	5.12 0.26	1.33 2.74	11460 513	6.1 3.2	33.7 13.4	3206 7
	930.14 6.58	571.13 19.13	1739126 2419	659.1 17.3	5302.1 60.6	510181 297

[a]Determined from $^{37}Cl(n,c,b)^{38}Ar$: Cl = 9.0159 ϑ 10^4.(^{38}Ar/b.J).(mole/mole); b = ((K/Cl).($^{38}Ar/^{39}Ar$))$_{Hb3gr}$; (K/Cl)$_{Hb3gr}$ = 5.242; b = 0.7946 0.3544.[b]Determined from $^{39K}(n,p)^{39}Ar$: K = (^{39}Ar/J).(K/^{40}K).(k/k$_e$).(mole/mole); k/k$_e$ = 9.58; K/^{40}K = 1.167 ϑ 10^4; J = 0.08018 0.00113 (1 sigma, excluding uncertainty on monitor ages). [c]Determined from $^{40}Ca(n,a)^{38}Ar$: Cl = 8.042 ϑ 10^4.(^{37}Ar/a.J).(mole/mole); a = ((K/Ca).($^{37}Ar/^{39}Ar$))$_{Hb3gr}$; (K/Ca)$_{Hb3gr}$ = 0.1674; a = 0.5422. [d]Represents analytical error and each step does not include uncertainties on the J value. [e]Calculated using the ratio of cosmogenic ^{38}Ar (from the relationship $38Ar_c$ = (5.35 ϑ ^{38}Ar-^{36}Ar)/(5.35–0.65): where 5.35 is the trapped $^{36}Ar/^{38}A$ solar wind ratio and 0.65 trapped $^{36}Ar/^{38}Ar$ cosmogenic ratio of Hennessy and Turner (1980) to the concentration of ^{37}Ar dervived from CaO content (calculated using [b] and [c]). $^{38}Ar_c/^{37}Ar$ ratios then provide apparent cosmic ray exposure (CRE) ages using the bulk sample chemistry, production rates of Eugster (1988). Errors reported include internal uncertainty on J [b] and assume a 10% error on the P38 value.

Cl ($9 10^{12}$)[a]		K ($9 10^{12}$)[b]		Ca ($9 10^{12}$)[c]								
Cum. ^{39}Ar (%)		^{40}Ar/^{39}Ar ratio		^{40}Ar/^{36}Ar of 0					Apparent Age (Ma)[d]		Exposure Age (Ma)[e]	
85	76	411.34	16.54	187249	5393	3.1	18.60	0.54	1645	31	21.7	11.6
137	122	1592.84	47.70	819576	23360	15.3	30.37	0.31	2223	13	7.7	2.3
177	158	1856.15	58.49	1036768	29572	29.5	57.52	0.82	3108	21	7.6	2.4
180	160	1678.17	52.98	999554	28504	42.4	76.24	1.10	3535	22	7.8	2.8
122	109	926.97	32.83	592954	16937	49.4	79.64	1.72	3603	34	8.8	4.0
139	124	1029.90	33.72	645864	18426	57.3	79.93	1.35	3609	26	8.7	4.0
152	135	1098.40	37.53	688475	19655	65.7	81.00	1.58	3629	30	8.9	3.3
150	134	1150.92	36.37	645646	18416	74.5	83.65	1.21	3680	23	9.4	3.5
103	92	810.96	24.57	436867	12453	80.7	84.25	0.96	3691	18	9.6	5.0
82	73	640.23	25.27	340165	9761	85.6	84.30	2.34	3692	44	9.9	5.4
88	78	704.64	23.68	395908	11306	91.0	83.74	1.55	3682	29	9.3	6.0
74	67	566.69	19.71	331281	9465	95.3	82.22	1.69	3653	32	9.7	7.2
13	12	88.28	13.64	57696	1885	96.0	79.35	12.06	3597	237	9.2	26.5
57	51	313.08	13.46	244917	7007	98.4	79.13	2.57	3593	51	10.3	8.5
38	34	176.48	12.33	173462	4999	99.8	77.39	4.95	3558	99	9.6	10.4
16	15	29.54	12.69	25446	1135	100.0	77.21	33.10	3555	666	29.8	61.7
1612	404	13074.59	128.82	7621828	64500							

ppm 17.97 4.50 ppm 160.75 1.58 wt % 13.44 0.11 (upper 58% of ^{39}Ar release) Fusion age (analytical error 3653 ± 11 (internal error) 3653 ± 45 (external error) 3653 ± 65 (upper 97.5% of ^{37}Ar release)

Plateau age (internal error) 8.4 1.0

Corrected for ^{40}Ar/^{36}Ar of 1

11	12	14.75	14.03	5115	979	0.3	38.69	18.40	2544	1296	97.9	438.7
27	25	57.97	16.65	20819	1288	1.3	49.21	7.03	2880	411	58.9	86.4
13	13	87.45	14.12	38652	1460	3.0	38.89	3.09	2550	217	13.7	53.8
29	26	147.01	13.97	71940	2245	5.7	63.33	2.88	3252	137	16.8	28.1
48	43	141.47	13.18	70075	2174	8.3	233.69	10.38	5374	152	17.6	32.4
10	9	107.42	8.53	58247	1746	10.3	98.29	3.65	3935	119	3.2	28.2
22	21	82.65	5.86	46559	1376	11.8	111.37	3.63	4136	106	18.4	49.5
33	30	161.83	10.15	96029	2803	14.8	95.10	2.67	3883	89	13.4	19.8
38	34	178.04	8.93	109315	3153	18.1	88.76	1.84	3773	66	13.3	20.4
20	19	99.62	9.78	61466	1865	20.0	91.01	4.28	3813	149	12.0	37.4
18	18	76.17	7.38	48478	1463	21.4	93.05	4.31	3848	147	15.2	47.9
17	17	83.00	12.02	51304	1672	22.9	100.34	7.12	3968	228	12.6	43.4
22	20	143.76	12.76	85970	2586	25.6	90.26	3.80	3800	133	8.9	20.0
36	32	235.38	12.12	141864	4099	29.9	90.83	1.96	3810	68	8.7	13.3
51	45	278.14	12.97	163854	4718	35.1	96.02	1.79	3898	59	11.1	10.8
153	136	993.80	34.32	593087	16939	53.5	94.21	0.95	3868	32	9.0	3.5
80	71	543.94	19.89	322518	9223	63.6	94.83	1.11	3878	37	8.6	5.7
149	133	1049.10	39.45	634771	18159	83.0	95.22	1.19	3885	40	8.4	3.3
73	65	499.55	18.54	310473	8878	92.2	96.06	1.16	3899	39	8.3	5.3
51	45	301.18	17.98	183430	5335	97.7	96.37	2.54	3904	84	9.7	8.8
21	19	89.15	11.11	55678	1752	99.4	95.17	5.78	3884	193	14.9	33.4
9	9	34.40	13.67	21026	1115	100.0	94.98	18.82	3881	631	16.8	87.7
930	242	5405.77	78.82	3190671	30079							

ppm 25.77 6.70 ppm 165.12 2.41 wt% 14.05 0.40 (upper 81% of ^{39}Ar release) Fusion age (analytical error) 3888 ± 19 (internal error) 49 (external error) Plateau age (analytical error) 3877± 16 (100% of ^{37}Ar release)

(internal error) 110 9.0 1.9

(external error) 160

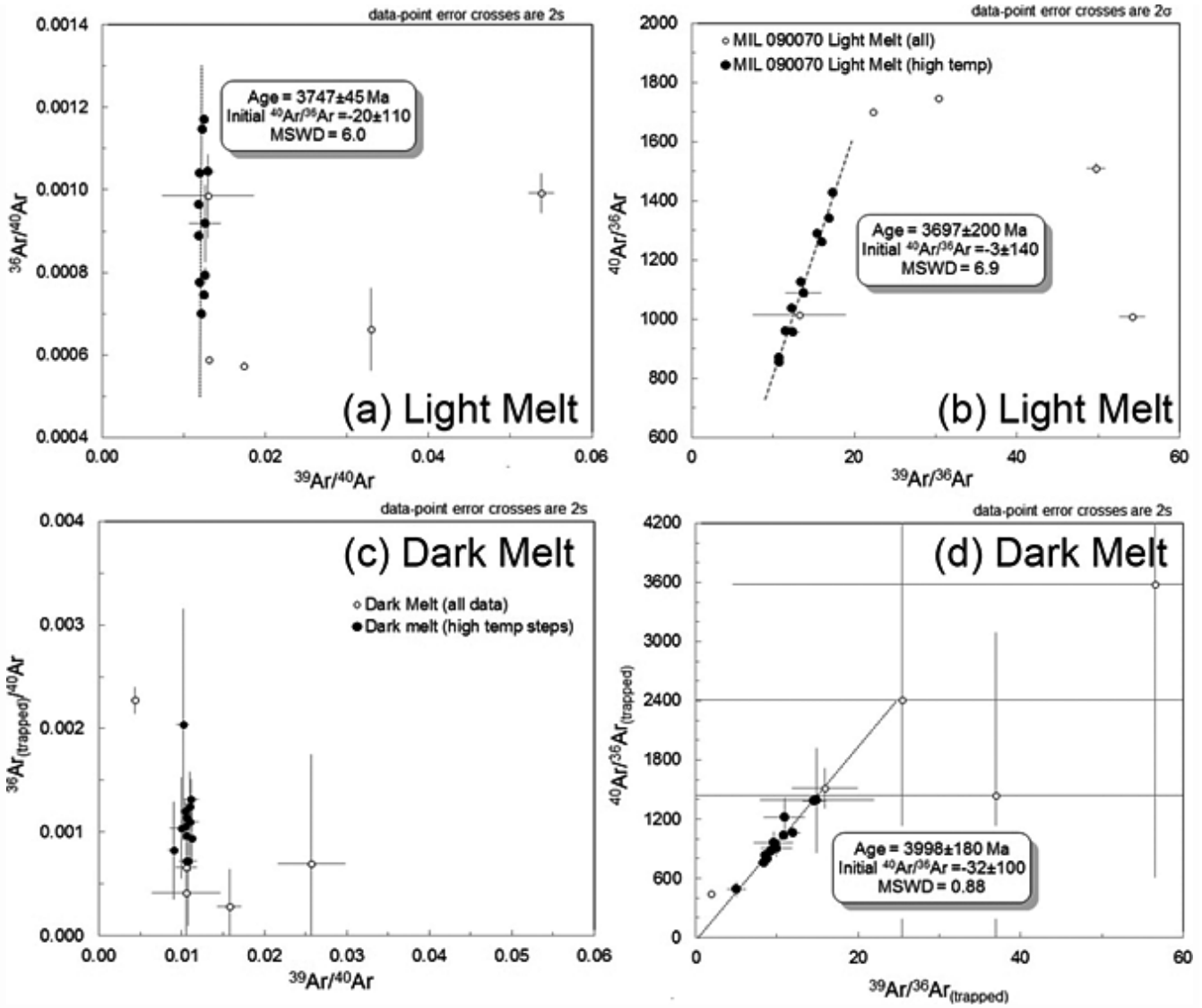

Fig. 8*. Inverse argon isotope isochron of $^{39}Ar/^{40}Ar$ versus $^{36}Ar/^{40}Ar$ ratios (a) and normal argon isotope isochron of $^{39}Ar/^{36}Ar$ versus $^{40}Ar/^{36}Ar$ ratios for MIL 090070,33 Light Melt Clast (b, data in Table 1). Inverse argon isotope isochron of $^{39}Ar/^{40}Ar$ versus $^{36}Ar/^{40}Ar$ (c) and normal argon isotope isochron of $^{39}Ar/^{36}Ar$ versus $^{40}Ar/^{36}Ar$ for MIL 090070,33 Dark Melt component (d) where $^{36}Ar_{(trapped)}$ refers to ^{36}Ar corrected for cosmogenic contribution (data in Table 1). Dashed line is a fit to bulk sample high temp steps (excluding final step), giving model isochron ages and initial $^{40}Ar/^{36}Ar$ ratios. Calculated isochron ages are not significant as data cluster at the radiogenic component.*

PAIRING RELATIONSHIPS

Both samples share similarities in terms of mineral chemistry and bulk-rock composition. However, results obtained from this study, together with previous analyses of other samples of these meteorites (Korotev et al. 2011; Liu et al. 2011; Shirai et al. 2012; Zeigler et al. 2012), indicate that there is no pairing relationship between them on the basis of bulk-rock composition. MIL 090070 may be grouped with two other Miller Range feldspathic samples MIL 090034 and MIL 090075 based on petrographic studies, bulk chemical composition, and ^{10}Be and ^{26}Al cosmogenic nuclide concentrations (Table 2) (Korotev et al. 2011; Liu et al. 2011; Shirai et al. 2012; Zeigler et al. 2012; Nishiizumi and Caffee 2013).

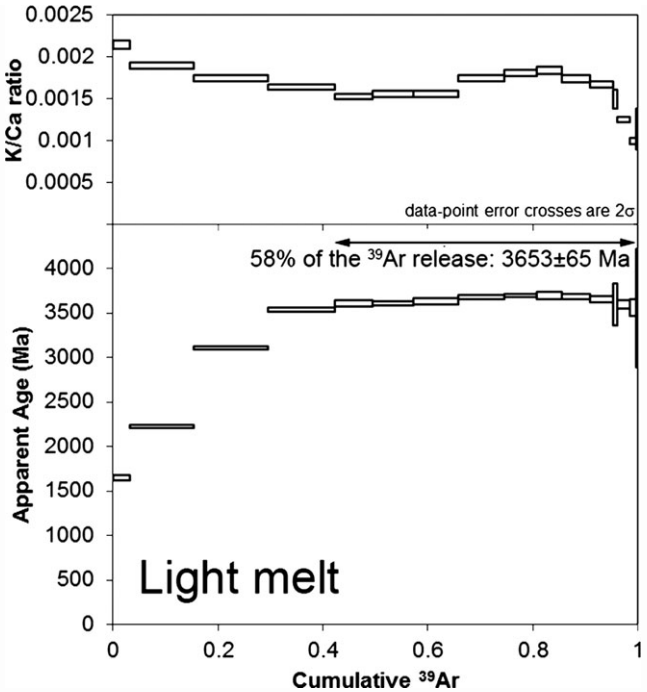

***Fig. 9**. Model age argon release profiles for the light melt component in MIL 090070. Top panel show K/Ca mole values derived from $^{39}Ar/^{37}Ar$ ratio released at each temperature step versus cumulative% of ^{39}Ar released from each step-heating. This is compared in the lower panels with the apparent ^{40}Ar-^{39}Ar age spectra where each box represents a single step release including a 2σ error. The age shown is a part fusion release age from 58% of the ^{39}Ar release.*

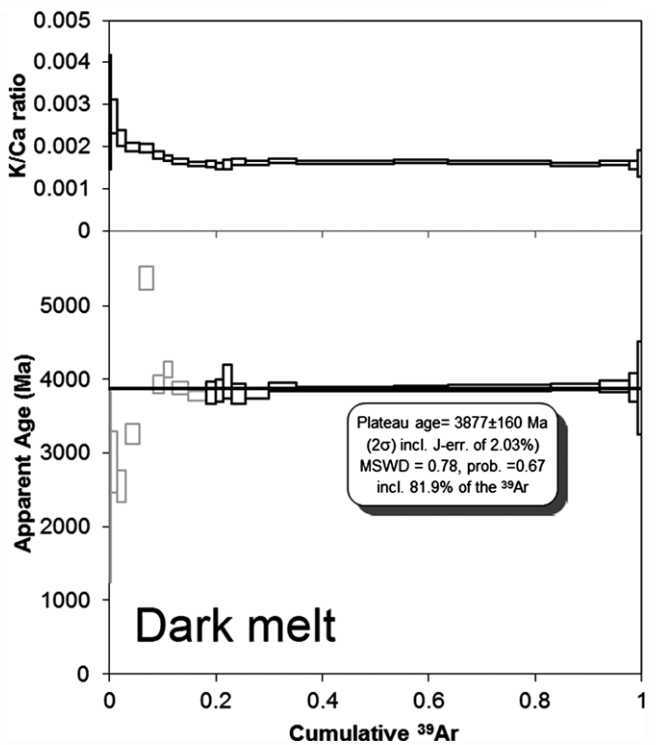

***Fig. 10**. Model age argon release profiles for the dark melt component in MIL 090070. Top panel show K/Ca mole values derived from $^{39}Ar/^{37}Ar$ ratio released at each temperature step versus cumulative% of ^{39}Ar released from each step-heating. This is compared in the lower panels with the apparent ^{40}Ar-^{39}Ar age spectra where each box represents a single step release including a 2σ error. Gray boxes represent those that are not included in the plateau age calculation. Plateau age reported includes external error on the monitor age.*

POTENTIAL LAUNCH SITES

Following the method described by Calzada-Diaz et al. (2015), global elemental abundance maps from Lunar Prospector gamma ray spectrometer (LP-GRS) measurements (Prettyman et al. 2006), together with measured average compositions of the samples (Table 1), were used to constrain their possible launch location(s). It is considered a match when all three of the FeO, TiO_2, and Th abundances of the average meteorite bulk compositions including an uncertainty on the data of 2σ standard deviation (Table 1) overlap with the ranges of the surface compositions measured by LP-GRS the instrument uncertainties for each measurement (Prettyman et al. 2006).

Results for MIL 090036 (Fig. 11) show that most of the matches are in the surroundings of the Procellarum KREEP Terrane (PKT), including near the Apollo 16 landing site. Other matches are located in the eastern area of Mare Frigoris and in the western part of the South Pole-Aitken (SPA) basin.

The bulk-rock FeO, TiO_2, and Th compositions of MIL 090070 were averaged together with its paired meteorites MIL 090034 and MIL 090075 (Korotev and Zeigler 2015). This average value, along with its standard deviation (Table 1), gives a more comprehensive view of the composition of the material from which it is derived. Several matches for the meteorite group were obtained, most of them in the farside Feldspathic Highlands Terrane (FHT) or in the Outer-Feldspathic Highlands Terrane (FHT-O; Fig. 11) (Korotev et al. 2011; Liu et al. 2011; Shirai et al. 2012; Zeigler et al. 2012).

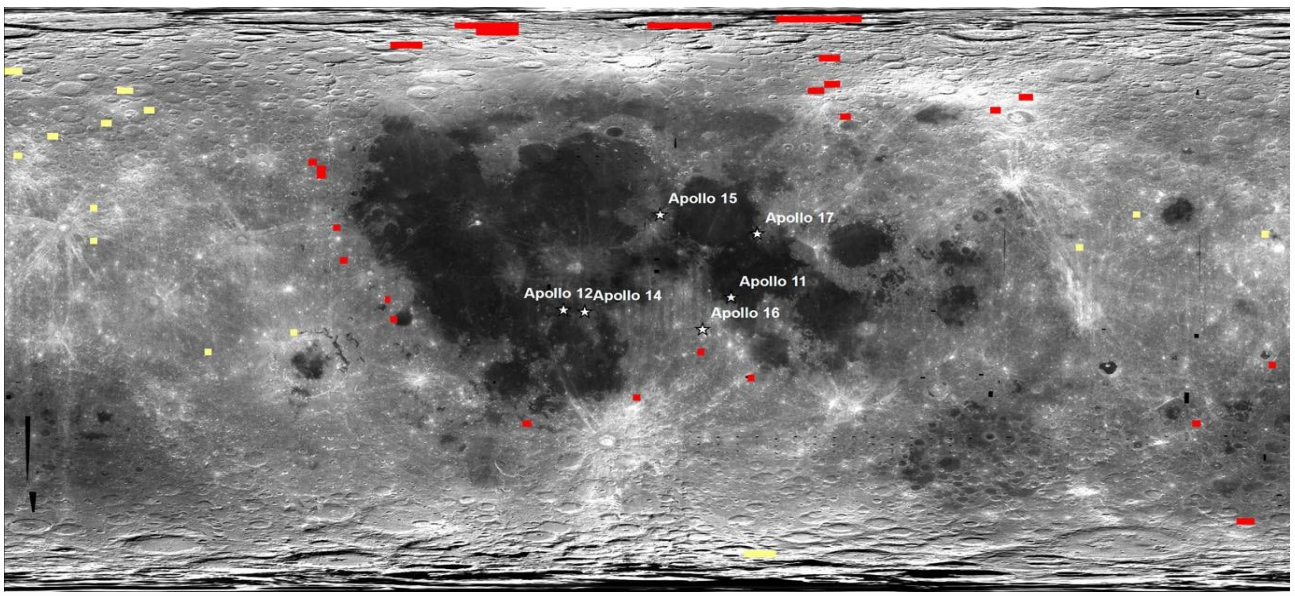

***Fig. 11**. Image showing the areas where surface regolith FeO, TiO_2, and Th composition measurements obtained by Lunar Prospector Gamma Ray Spectrometer (Prettyman et al. 2006) match the analytical composition of regolith breccias MIL 090036 in red and MIL 090070 and paired stones MIL 090034 and MIL 090071 (Korotev and Zeigler 2015) in yellow (Table 2). Underlying albedo image of the Moon is a Clementine albedo map in a cylindrical projection with 0° longitude in the center.*

DISCUSSION

Geological Record Preserved in MIL 090036

MIL 090036 is unusual among Al-rich feldspathic lunar meteorites because of the KREEP signature bulk composition. The most similar other lunar meteorite is North West Africa (NWA) 4936, which contains 1.95 ppm Th and 6.22 ppm Sm (Korotev et al. 2009).

Previous petrographic and chemical studies of MIL 090036 (Korotev et al. 2011; Shirai et al. 2012) have suggested similarities with returned samples from the Apollo 16 landing site (Jerde et al. 1987; Korotev 1997). The KREEPy component of MIL 090036 is comparable to that observed in Apollo 16 samples as shown by its similar Th content (Table 2). Our investigation of remote sensing data (Fig. 11) also suggests the Apollo 16 area of the Cayley Highlands as a potential launch site. However, its bulk-rock REE pattern (Fig. 7) differs from the pattern for averaged bulk-rock Apollo 16 soils and regolith breccias (McKay et al. 1986; Jerde et al. 1987; Lucey et al. 2006). The discrepancy is most obvious in the Eu abundances. The Eu anomaly is calculated using et al. 1986; Jerde et al. 1987; Lucey et al. 2006). Small sample size (150 mg) of the chips used in the bulk- rock analysis in this study (typical for modern meteorite research) makes, however, direct comparison with average composition difficult.

The mineral chemistry of components in different clast types (impact-melt breccia matrices, impact melts, and granulitic) in MIL 090036 are intermediate between the composition of the pristine lunar highlands ferroan anorthosite suite and low Mg# (~60–70) samples in the magmatic Mg-Suite (Fig. 3). They are similar in

composition to the Apollo 16 average impact-melt compositions of KREEP-bearing groups 2DB and 2NR (Korotev 2000; Fig. 3).

The formula $Eu/Eu^{*} = \frac{Eu_{CN}}{\sqrt{Sm_{CN} + Gd_{CN}}}$ where CN= chondrite-normalized (using the values of Anders and Grevesse (1989) was used to calculate the Eu anomaly. A larger negative Eu anomaly (Eu/Eu* 0.3) is observed on the Apollo 16 bulk soil REE pattern, compared to MIL 090036,34 (Eu/Eu* 0.05; Fig. 7). This discrepancy may result from the difference in mare basalt or KREEP components found at the Apollo 16 site and MIL 090036: our study and that of Lanfang et al. (2014) did not identify any mare basalt lithological debris, whereas mafic impact-melt rocks are common in samples from all stations within the Apollo 16 landing site lithologies from the ferroan anorthosites and Mg-suite, and is most similar to plagioclase found in the ancient high-alkali magmatic rock suite (Fig. 3). An alkaline plagioclase fragment is part of an impact metlt clast. However, this plagioclase clast shows greater bulk Na_2O content (~4.3 wt%) than those compiled for anorthositic alkaline rocks from the Apollo 12 and 14 landing sites by Papike (1998; Na_2O <2.14 wt%). However, CaO content is slightly higher in the anorthositic alkaline rocks from the Apollo collection, ~15.8 wt% in contrast with ~12.4 wt% obtained during this analysis. Alkaline rocks are known to have high concentration of incompatible trace elements compared with Apollo ferroan anorthositic rocks (Snyder et al. 1995). The presence of high alkaline anorthositic clasts ($An_{59–63}$) may be the cause of the enhanced KREEPy signature within MIL 090036. This is linked to a potential origin of MIL 090036 in the surroundings outskirts of the PKT (Fig. 11) since the sample contains material similar from the high-alkali suite.

Reported $^{39}Ar/^{40}Ar$ ages (summarized in Fig. 11) suggest that the last major argon isotope resetting event in MIL 090036 took place at ~3.54 Ga (Park et al. 2013; Nyquist et al. 2016). MIL 090036 has a cosmic ray exposure of ~50 10 Ma (Nishiizumi and Caffee 2013; Park et al. 2013). This suggests that this sample was ejected from the lunar near-subsurface (depths ~100 cm) and it had a short transit time, arriving on the Earth as a meteorite 0.1–0.2 Ma ago.

Geological Records of MIL 090070

The high Al_2O_3 abundance (30.72 wt%), low Mg# (61.07), and low Sc content (6.81 ppm) of this sample are unusual among lunar highland meteorites. High bulk-rock Al_2O_3 contents and low Sc concentrations (Table 2) support our petrographic observations that the meteorite has high modal abundance of plagioclase and low abundances of mafic components (Fig. 1).

The bulk-rock REE composition of MIL 090070 (Table 2) is similar to the upper portion of the anorthositic crust (Fig. 7). In terms of mineral chemistry, An# versus Mg#, most impact-melt breccia clasts and the MIL 090070 matrix have mineral compositions that are most similar to samples from the Apollo ferroan anorthosite suite (Fig. 6). However, some poikiloblastic impact-melt clasts plot in the area between the ferroan anorthositic and the high-magnesium suites, indicating that these clasts may have experienced some degree of mixing, similar to that previously observed in other feldspathic lunar meteorites (Cahill et al. 2004).

It has been suggested that farside lunar highland anorthosites are more Mg-rich than ferroan anorthosites from the Apollo 16 site (Takeda et al. 2006; Arai et al. 2008) with significant implications for lunar crustal evolution (Arai et al. 2008; Gross et al. 2014; Pernet- Fisher and Joy 2016). Major element composition of plagioclase in MIL 090070 (Fig. 6) indicates that anorthositic fragments from this sample were derived from a ferroan anorthosite type protolith that probably originated during crust formation in the early lunar history (Taylor and McLennan 2009; Elkins-Tanton et al. 2011). However, Sm-Nd trace element analysis of MIL 090070 plagioclase by Nyquist et al. (2016) suggests that this parent anorthosite protolith was formed from a REE-rich melt that then gave rise to the Apollo FANs and magnesian anorthosite meteorite Dhofar 489. This is consistent with other studies of lunar meteorite plagioclase (Cahill et al. 2004; Russell et al. 2014), suggesting that there is heterogeneity in parent magmas of the anorthositic crustal units distributed across the Moon (Pernet-Fisher and Joy 2016). The anorthositic protolith was highly disrupted by impact bombardment (see below) and extensively reworked, although still preserves compositional evidence of a ferroan anorthosite parent rock affinity.

We have observed that most of the FeO, TiO_2, and Th similarities to compositions of the regolith are within the northern farside of the Moon, although there are some limb locations from which this sample could be originated (Fig. 11). Based on the number of results, our interpretation is that MIL 090070 is probably derived from the lunar farside highlands (Fig. 11), suggesting that at least part of the lunar farside crust may contain a mix of ferroan anorthosites as sampled by MIL 090070, and magnesian feldspathic rocks as mapped out in this area from orbit (Arai et al. 2005; Takeda et al. 2006; Gross et al. 2014; Crites and Lucey 2015). This interpretation has implications for understanding the diversity and formation of the lunar crust (Pernet-Fisher and Joy 2016), suggesting that both ferroan and magnesian anorthosites may coexist in a geographically similar region and are sampled by different feldspathic lunar meteorites (Korotev et al. 2003; Day et al. 2006; Gross et al. 2014).

A major impact event occurred to the MIL 090070 parent crust at ~3.9 Ga, recorded by the Pb isotope (Bouvier et al. 2013) and Ar isotope reset systems (this study—see Fig. 12). This is similar in age to the timing of the nearside Imbrium impact event (~3.9 Ga: Hartmann et al. 1981; Neukum and Ivanov 1994; Snape et al. 2015) at the end

of the basin-forming era (Stöffler et al. 2006). The argon isotope resetting event at 3.9 Ga may represent the time of the impact that excavated into the protolith anorthositic crust, shocking the mineral debris (Martin et al. 2016), and assembling the feldspathic impact-melt breccias that we see in the sample (Fig. 5), or it may represent the final assembly of the whole sample into a breccia.

Secondary impact events are recorded in the argon isotope system from 3.9 to ~3 Ga and induced local degassing events in some of the components of the sample (Fig. 12) (Park et al. 2013). The pale clast we have measured gives a younger resetting age than the dark glassy impact melt (Fig. 12). This could be explained by preferential degassing from heavily fractured rock components (i.e., shocked impact-melt breccia that have more grain boundaries) within the pale clast feldspathic impact-melt breccia component (Figs. 5a–c). These ages (and that recorded by MIL 090036: Park et al. 2013) are consistent with the $^{39}Ar/^{40}Ar$ dates recorded in impact melts in feldspathic lunar meteorites, which show a range of resetting ages between 2.76 and 3.92 Ga (Cohen et al. 2000, 2004; Nyquist et al. 2006; Fernandes et al. 2013; and references therein) after the timing of major basin- formation events (see summary by Joy and Arai 2013). The sample does not contain solar wind implanted isotopes, indicating that it remained in the lunar subsurface (upper few meters of the crust) and underwent a short transit time since it was ejected, arriving to the Earth ~0.7 Ma ago (Nishiizumi and Caffee 2013).

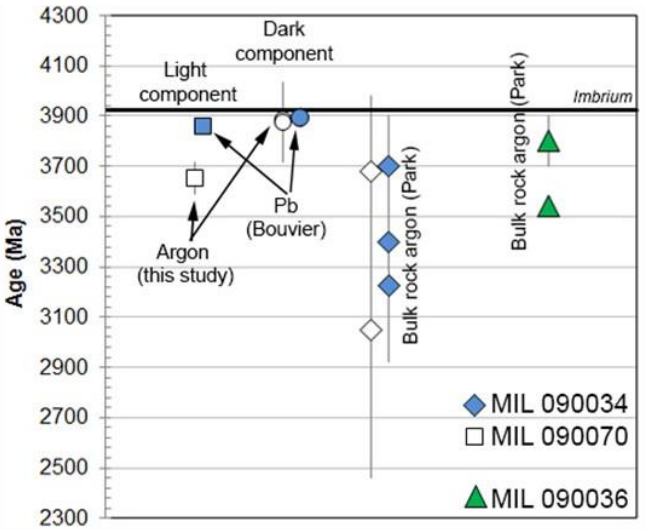

Fig. 12. *Summary of events recorded by argon and Pb isotopes for components and bulk-rock samples of MIL 090034 (Bouvier et al. 2013; Park et al. 2013), MIL 090070 (Park et al. 2013; Bouvier et al. 2013; and this study). Park et al. (2013) determined argon isotope plateau and normal isochron age models. Bouvier et al. (2013) report Pb isotopes. The data from this study reflect argon fusion ages and a plateau age (Table 1). Error bars to our data are 2σ external errors (Table 1), and other errors are as reported from literature sources (no error bar implies error is smaller than symbol size). Age of the Imbrium basin-forming event is shown for reference using the reported age of Snape et al. (2015) of 3915 Ma.*

SUMMARY

MIL 090036,34 is a feldspathic immature (i.e., having experienced only a short exposure at the lunar surface; McKay et al. 1991) regolith breccia (26.72 wt% Al_2O_3, 5.27 wt% FeO) with a KREEPy signature (1.89 ppm Th) probably related to a high alkali component within the impact-melt breccia clasts. It has suffered metamorphism as indicated by the presence of granulite breccias and rare plagioclase transformed into glass. Petrography and bulk-rock major element composition shows some similarities with regolith and soils from the Apollo 16 landing area. However, Sc and Eu/Eu* in MIL 090036,34 show some discrepancies with soils from Apollo 16 samples.

MIL 090070,35 is also a feldspathic immature regolith breccia (30.72 wt% Al_2O_3, 3.77 wt% FeO) and low Th abundance (0.44 ppm), formed of plagioclase, pyroxenes, and olivine mineral fragments and impact-melt breccia clasts of feldspathic composition, all embedded in a glassy feldspathic matrix. Bulk-rock major, minor, and trace elements agree with a ferroan anorthositic lunar crust composition. An impact formation event degassed the older MIL 090070 FAN protolith mineral and rock components at ~3.9 Ga, as suggested by the ages obtained from the darker glassy material. Subsequent impacts induced local degassing events in the components of the sample, probably due to differences in their texture (i.e., fragmented impact-melt breccias with more grain boundaries are degassed more).

Bulk-rock FeO, TiO_2, and Th measurements on both samples were compared with LP-GRS data sets to determine areas of the lunar surface where the regolith composition matches the abundances observed in the sample. MIL 090036 compositions match with those of the regolith surrounding the PKT, including the Apollo 16 landing area. In contrast, the MIL 090070 composition shows that the feldspathic highlands terrane in the far side of the Moon as the most likely source of this meteorite, indicating that this terrane is composed of both ferroan and magnesian anorthosites as sampled by different lunar feldspathic meteorites.

Acknowledgments—Thanks to NASA for the ANSMET sample loan and to the 2009 field team for collecting the samples. We thank Drs. John Spratt, Anton Kearsley, and Andrew Beard for assistance with electron microprobe and SEM techniques, Dr. Louise Alexander for her advice and support, and Professor Hilary Downes for comments on an earlier version of this manuscript. We thank Drs. John Cowpe, Ray Burgess, Patricia Clay, and Lorriane Ruzie for assistance with argon techniques. We also thank Drs. Georgiana Kramer and Karen Stockstill-Cahill for their helpful reviews and recommendations, and the handling editor Dr. Cyrena Goodrich for her review. A.C.D. and I.A.C. thank STFC (through grant ST/K000829/1) for funding. K.J. thanks STFC (ST/J001643/1 and ST/L002957/1) and a Royal Society University Research Fellowship (RS/UF140190) at the University of Manchester.

REFERENCES

Anders E. and Grevesse N. 1989. Abundances of the elements: Meteoritic and solar. Geochimica et Cosmochimica Acta 53:197–214.

Arai T., Misawa K., and Kojima H. 2005. A new lunar meteorite MET 01210: Mare breccia with a low-Ti ferrobasalt (abstract #2361). 36th Lunar and Planetary Science Conference. CD-ROM.

Arai T., Takeda H., Yamaguchi A., and Ohtake M. 2008. A new model of lunar crust: Asymmetry in crustal omposition and evolution. Earth, Planets and Space 60:433–444.

Basilevsky A. T., Neukum G., and Nyquist L. 2010. The spatial and temporal distribution of lunar mare basalts as deduced from analysis of data for lunar meteorites. Planetary and Space Science 58:1900–1905.

Bouvier A., Romaniello S. J., Wadhwa M., Korotev R. L., and Hartmann W. K. 2013. Pb-Pb dating of Apollo 67016 and MIL 090034 lunar impact breccias (abstract #5312). 76th Annual Meteoritical Society Meeting. Meteoritics & Planetary Science 48.

Cahill J. T., Floss C., Anand M., Taylor L. A., Nazarov M.A., and Cohen B. A. 2004. Petrogenesis of lunar highlands meteorites: Dhofar 025, Dhofar 081, Dar al Gani 262, and Dar al Gani 400. Meteoritics & Planetary Science 39:503–529.

Calzada-Diaz A., Joy K. H., Crawford I. A., and Nordheim T. A. 2015. Constraining the source regions of lunar meteorites using orbital geochemical data. Meteoritics & Planetary Science 15:214–228.

Cohen B. A., Swindle T. D., and Kring D. A. 2000. Support for the lunar cataclysm hypothesis from lunar meteorite impact melt ages. Science 290:1754–1756.

Cohen B. A., James O. B., Taylor L. A., Nazarov M. A., and Barsukova L. D. 2004. Lunar highland meteorite Dhofar 026 and Apollo sample 15418: Two strongly shocked, partially melted, granulitic breccias. Meteoritics & Planetary Science 39:1419–1447.

Crites S. T. and Lucey P. G. 2015. Revised mineral and Mg# maps of the Moon from integrating results from the Lunar Prospector neutron and gamma-ray spectrometers with Clementine spectroscopy. American Mineralogist 100:973–982.

Day J. M. D., Taylor L. A., Floss C., Patchen A. D., Schnare D. W., and Pearson D. G. 2006. Comparative petrology, geochemistry, and petrogenesis of evolved, low-Ti lunar mare basalt meteorites from the LaPaz Icefield, Antarctica. Geochimica et Cosmochimica Acta 70:1581–1600.

Elkins-Tanton L. T., Burgess S., and Yin Q. Z. 2011. The lunar magma ocean: Reconciling the solidification process with lunar petrology and geochronology. Earth and Planetary Science Letters 304:326–336.

Eugster O. 1988. Cosmic-ray production rates for 3He, 21Ne, 38Ar, 83Kr, and 126Xe in chondrites based on 81Kr-Kr exposure ages. Geochimica et Cosmochimica Acta 52:1649–1662.

Fagan A. L., Joy K. H., Bogard D. D., and Kring D. A. 2014. Ages of globally distributed lunar paleoregoliths and soils from 3.9 Ga to the present. Earth, Moon, and Planets112:59–71.

Fernandes V. A., Fritz J., Weiss B. P., Garrick-Bethell I., and Shuster D. L. 2013. The bombardment history of the Moon as recorded by 40 Ar-39 Ar chronology. Meteoritics & Planetary Science 48:241–269.

Gillis J. J., Jolliff B. L., and Korotev R. L. 2004. Lunar surface geochemistry: Global concentrations of Th, K, and FeO as derived from Lunar Prospector and Clementine data. Geochimica et Cosmochimica Acta68:3791–3805.

Gross J., Treiman A. H., and Mercer C. N. 2014. Lunar feldspathic meteorites: Constraints on the geology of the lunar highlands, and the origin of the lunar crust. Earth and Planetary Science Letters 388:318–328.

Hartmann W. K., Strom R. G., Weidenschilling S. J., Balsius K. R., Woronow A., Dence M. R., Grieve R. A. F., Diaz J., Chapman C. R., Shoemaker E. M., and Jones K. L.1981. Chronology of planetary volcanism by c omparative studies of planetary craters. In Basaltic volcanism on the terrestrial planets, edited by Basaltic Volcanism Study Project. Houston, Texas: Pergamon Press. pp. 1049–1128.

Hennesy J., and Turner G. 1980. ^{40}Ar-^{39}Ar ages and irradiation history of Luna 24 basalts. Philosophical Transactions of the Royal Society London A297:27–39.

Jerde E. A., Warren P. H., Morris R. V, Heiken G. H., and Vaniman D. T. 1987. A potpourri of regolith breccias: "New" samples from the Apollo 14, 16, and 17 landing sites. Proceedings of the 17th Lunar and Planetary Science Conference, Part 2. Journal of Geophysical Research 92: E526–E536.

Jolliff B. L. 1998. Large-scale separation of K-fractionation and REEP- fractionation in the source regions of Apollo impact-melt breccias, and a revised estimate of the KREEP composition. International Geology Review 40:916–935.

Jolliff B. L., Wieczorek M. A. , Shearer C. K., and Neal C.R.2006. New views of the Moon. Reviews in mineralogy & geochemistry, Chantilly, Virginia: Mineralogical Society of America 60:129–222.

Joy K. H. and Arai T. 2013. Lunar meteorites: New insights into the geological history of the Moon. Astronomy & Geophysics 54:4–28.

Joy K. H., Crawford I. A., Russell S. S., and Kearsley A. T. 2010. Lunar m e t e o r i t e r e g o l i t h b r e c c i a s: An in situ study of impact melt composition using LA-ICP-MS with implications for the composition of the lunar crust. Meteoritics & Planetary Science 45:917–946.

Joy K. H., Burgess R., Hinton R., Fernandes V. A., Crawford I. A., Kearsley A. T., and Irving A. J. 2011a. Petrogenesis and chronology of lunar meteorite Northwest Africa 4472: A KREEPy regolith breccia from the Moon. Geochimica et Cosmochimica Acta 75:2420–2452.

Joy K. H., Kring D. A., Bogard D. D., McKay D. S., and Zolensky M. E. 2011b. Re-examination of the formation ages of the Apollo 16 regolith breccias. Geochimica et Cosmochimica Acta 75:7208–7225.

Joy K. H., Ross D. K., Zolensky M. E., and Kring D. A. 2011c. Reconnaissance element mapping of lunar regolith breccias. Annual Meeting of the Lunar Exploration Analysis Group.

Korotev R. L. 1996. On the relationship between the Apollo 16 ancient regolith breccias and feldspathic fragmental breccias, and the composition of the prebasin crust in the Central Highlands of the Moon. Meteoritics & Planetary Science 31:403–412.

Korotev R. L. 1997. Some things we can infer about the Moon from the composition of the Apollo 16 regolith. Meteoritics & Planetary Science 32:447–478.

Korotev R. L. 2000. The great lunar hot spot and the composition and origin of the Apollo mafic ("LKFM") impact-melt breccias. Journal of Geophysical Research 105:4317–4345.

Korotev R. L. 2005. Lunar geochemistry as told by lunar meteorites. Chemie der Erde—Geochemistry 65:297–346.

Korotev R. L. and Zeigler R. A. 2015. ANSMET meteorites from the Moon. In 35 seasons of U.S. Antarctic meteorites, edited by Righter K., Corrigan C. M., McCoy T. J., and Harvey R. Washington, D.C.: American Geophysical Union. pp. 101–130.

Korotev R. L., Jolliff B. L., Zeigler R. A., Gillis J. J., and Haskin L. A. 2003. Feldspathic lunar meteorites and their implications for compositional remote sensing of the lunar surface and the composition of the lunar crust. Geochimica et Cosmochimica Acta 67:4895–4923.

Korotev R. L., Zeigler R. A., Jolliff B. L., Irving A. J., and Bunch T. E. 2009. Compositional and lithological diversity among brecciated lunar meteorites of intermediate iron concentration. Meteoritics & Planetary Science 44:1287–1322.

Korotev R. L., Jolliff B. L., and Carpenter P. K. 2011. Miller Range feldspathic lunar meteorites (abstract #1999). 42ndLunar and Planetary Science Conference. CD-ROM.

Lanfang X., Hongyi C., Bingkui M., Zhipeng X., and Jie Y. 2014. Petrography and mineralogy of new lunar meteorite MIL 090036. Advances in Polar Science 25:17–25.

Liu Y., Patchen A., and Taylor L. A. 2011. Lunar Highland breccias MIL 090034/36/70/75: A significant KREEP component (abstract #1261). 42nd Lunar and Planetary Science Conference. CD-ROM.

Lucey P. G., Korotev R. L., Gillis J. J., Taylor L. A., Lawrence D., Campbell B. A., Elphic R., Feldman B.,Hood L. L., Hunten D., Mendillo M., Noble S., Papike J. J., Reedy R. C., Lawson S., Prettyman T., Gasnault O., and Maurice S. 2006. Understanding the lunar surface and space-moon interactions. In New views of the Moon, edited by Jolliff B. L., Wieczorek M. A., Shearer C. K. and Neal C. R. Reviews in mineralogy & geochemistry vol. 60. Chantilly, Virginia: Mineralogical Society of America. pp.83–219.

Ludwig K. R. 2012. User's manual Isoplot v3.75. A geochronological toolkit for Microsoft Excel. Berkeley Gechronology Center Special Publication 5.

Martin D. J. P., Joy K. H., Wogelius R., Morlok A., and Hiesinger H. 2016. Using quantitative micro-FTIR spectroscopy to characterise the shock history of feldspathic lunar meteorites Miller Range 090034, 090070 and 090075 (abstract #1547). 47th Lunar and Planetary Science Conference. CD-ROM.

McKay D. S., Bogard D. D., Morris R. V., Korotev R. L., Johnson P., and Wentworth S. J. 1986. Apollo 16 regolith breccias: Characterization and evidence for early formation in the mega-regolith. Journal of Geophysical Research: Proceedings of the Sixteenth Lunar and Planetary Science Conference 91:D277–D303.

McKay D. S., Heiken G. H., Basu A., Blandford G., Simon S., Reedy R., French B. M., and Papike J. J. 1991. The lunar regolith. In The lunar sourcebook, edited by Heiken G. H., Vaniman D. T., and French B. M. New York: Cambridge University Press. pp. 285–356.

Neukum G. and Ivanov B. A. 1994. Crater size distribution and impact probabilities on Earth from lunar terrestrial- planet and asteroid cratering data. In Hazards due to comets and asteroids, edited by Gehrels T. Tucson, Arizona: University of Arizona Press. pp. 359–416.

Nishiizumi K. and Caffee M. W. 2013. Relationships among six lunar meteorites from Miller Range, Antarctica based on cosmogenic radionuclides (abstract #2715). 44th Lunar and Planetary Science Conference. CD-ROM.

Nyquist L., Bogard D., Yamaguchi A., Shih C. -Y., Karouji Y., Ebihara M., Reese Y., Garrison D., McKay G., and Takeda H. 2006. Feldspathic clasts in Yamato-86032: Remnants of the lunar crust with implications for its formation and impact history. Geochimica et Cosmochimica Acta 70:5990–6015.

Nyquist L. E., Shirai N., Yamaguchi A., Shih C.-Y., Park J., and Ebihara M. 2016. Feldspathic meteorites MIL 090034 and 090070: Late additions to the lunar crust (abstract #1521). 47th Lunar and Planetary Science Conference. CD- ROM.

Palme H., Spettel B., Jochum K. P., Dreibus G., Weber H., Weckwerth G., Wanke H., Bischoff A., and Stöffler D. 1991. Lunar highland meteorites and the composition of the lunar crust. Geochimica et Cosmochimica Acta 55:3105–3122.

Papike J. J. 1998. Comparative planetary mineralogy: Chemistry of melt-derived pyroxene, feldspar, and olivine. In Planetary materials, edited by Papike J. J. Reviews in Mineralogy, vol. 36. Washington D.C.: Mineralogical Society of America. pp. 7-01–7-12.

Papike J. J., Karner J. M. and Shearer C. K. 2003. Determination of planetary basalt parentage: A simple technique using the electron microprobe. American Mineralogist 88:469–472.

Park J., Nyquist L. E., Shih C. -Y., Herzog G. F., Yamaguchi A., Shirai N., Ebihara M., Lindsay F. N., Delaney J., Turrin B. and Swisher III C. 2013. Late bombardment ofthe lunar highlands recorded in MIL 090034, MIL 090036 and MIL 090070 lunar meteorites (abstract #2576). 44th Lunar and Planetary Science Conference. CD-ROM.

Pernet-Fisher J. and Joy K. H. 2016. The lunar highlands: Old crust, new ideas. Astronomy & Geophysics 57:26–30.

Prettyman T. H., Hagerty J. J., Elphic R. C., Feldman W. C., Lawrence D. J., McKinney G. W., and Vaniman D. T. 2006. Elemental composition of the lunar surface: Analysis of gamma ray spectroscopy data from Lunar Prospector. Journal of Geophysical Research 111:E12007.

Renne P. R., Mundil R., Balco G., Min K., and Ludwig K.R. 2010. Joint determination of ^{40}K decay constants and 40Ar*/40K for the Fish Canyon sanidine standard, and improved accuracy for $^{40}Ar/^{39}Ar$ geochronology. Geochimica et osmochimica Acta 74:5349–5367.

Righter K. 2010. Antarctic Meteorite Newsletter 33(2).

Russell S. S., Joy K. H., Jeffries T. E., Consolmagno G. J., and Kearsley A. 2014. Heterogeneit in lunar anorthosite meteorites: Implications for the lunar magma ocean model. Philosophical Transactions. Series A, Mathematical, Physical, and Engineering Sciences 372:20130241.

Shirai N., Ebihara M., Sekimoto S., Yamaguchi A., Nyquist L., Shih C.-Y., Park J., and Nagao K. 2012. Chemical characteristics of MIL 090034, 090036 and 090070 (abstract #1659). 43rd Lunar and Planetary Science Conference. CD-ROM.

Snape J. F., Joy K. H., and Crawford I. A. 2011.Characterization of multiple lithologies within the lunar feldspathic regolith breccia meteorite Northeast Africa 001. Meteoritics & Planetary Science 46:1288–1312.

Snape J. F., Nemchin A. A., Thiessen F., Bellucci J. J., and Whitehouse M. J. 2015. The impact history of the Moon: Implications of new high-resolution U-Pb analyses of Apollo impact breccias. Geophysical Research Abstracts 17:11373.

Snyder G. A., Lawrece T. A., and Hallyday A. N. 1995. Chronology and petrogenesis of the lunar highlands alkali suite: Cumulates from KREEP basalt crystallization. Geochimica et Cosmochimica Acta 59:1185–1203.

Spray J. G. 2016. Lithification mechanisms for planetary regoliths: The glue that binds. Annual Review of Earth and Planetary Sciences 44:139–174.

Stöffler D., Ryder G., Ivanov B. A., Artemieva N. A., Cintala M.J., and Grieve R. A. 2006. Cratering history and lunar chronology. In New views of the Moon, edited by Jolliff B. L., Wieczorek M. A., Shearer C. K. and Neal C. R. Chantilly, Virginia: Mineralogical Society of America. pp. 519–596.

Takeda H., Yamaguchi A., Bogard D., Karouji Y., Ebihara M., Ohtake M., Saiki K., and Arai T. 2006. Magnesian anorthosites and a deep crustal rock from the farside crust of the moon. Earth and Planetary Science Letters 247:171–184.

Taylor S. R. and McLennan S. M. 2009. Planetary crusts: Their composition, origin and evolution. Cambridge, UK: Cambridge Planetary Science.

Warren P. H. 1994. Lunar and Martian meteorite delivery services. Icarus 111:338–363.

Warren P. H., Ulff-Møller F., and Kallemeyn G. W. 2005. "New" lunar meteorites: Impact melt and regolith breccias and large-scale heterogeneities of the upper lunar crust. Meteoritics & Planetary Science 40:989–1014.

Wieler R. 2016. Do lunar and meteoritic archives record temporal variations in the composition of solar wind noble gases and nitrogen? A reassessment in the light of Genesis data Chemie der Erde—Geochemistry:1–18.

Zeigler R. A., Korotev R. L., and Jolliff B. L. 2012. Pairing relationships among feldspathic lunar meteorites from Miller Range, Antarctica (abstract #2377). 43rd Lunar and Planetary Science Conference. CD-ROM.